



HAL
open science

Scanless two-photon voltage imaging

Ruth Sims, Imane Bendifallah, Christiane Grimm, Aysha Lafirdeen, Xiaoyu Lu, François St-Pierre, Eirini Papagiakoumou, Valentina Emiliani

► **To cite this version:**

Ruth Sims, Imane Bendifallah, Christiane Grimm, Aysha Lafirdeen, Xiaoyu Lu, et al.. Scanless two-photon voltage imaging. Research Square - Preprint, 2023, Online ahead of print. 10.21203/rs.3.rs-2412371/v1 . inserm-04251506

HAL Id: inserm-04251506

<https://inserm.hal.science/inserm-04251506>

Submitted on 20 Oct 2023

HAL is a multi-disciplinary open access archive for the deposit and dissemination of scientific research documents, whether they are published or not. The documents may come from teaching and research institutions in France or abroad, or from public or private research centers.

L'archive ouverte pluridisciplinaire **HAL**, est destinée au dépôt et à la diffusion de documents scientifiques de niveau recherche, publiés ou non, émanant des établissements d'enseignement et de recherche français ou étrangers, des laboratoires publics ou privés.



Distributed under a Creative Commons Attribution 4.0 International License

Scanless two-photon voltage imaging

Ruth Sims (✉ ruth.sims@inserm.fr)

Institut de la Vision

Imane Bendifallah (✉ imane.bendifallah@inserm.fr)

Institut de la Vision <https://orcid.org/0000-0003-4576-0903>

Christiane Grimm (✉ christiane.grimm@inserm.fr)

Institut de la Vision <https://orcid.org/0000-0002-2407-6152>

Aysha Lafirdeen (✉ aysha.mohamed-lafirdeen@inserm.fr)

Institut de la Vision

Xiaoyu Lu (✉ xiaoyu.lu@rice.edu)

Rice University <https://orcid.org/0000-0003-2426-1427>

François St-Pierre (✉ Francois.St-Pierre@bcm.edu)

Rice University

Eirini Papagiakoumou (✉ eirini.papagiakoumou@inserm.fr)

The Vision Institute <https://orcid.org/0000-0002-7333-8796>

Valentina Emiliani (✉ valentina.emiliani@inserm.fr)

Vision Institute, Sorbonne Univ. <https://orcid.org/0000-0003-2992-9510>

Article

Keywords:

DOI: <https://doi.org/>

License:   This work is licensed under a Creative Commons Attribution 4.0 International License.

[Read Full License](#)

Additional Declarations: There is **NO** Competing Interest.

1 Scanless two-photon voltage imaging

2
3 Ruth R. Sims*¹, Imane Bendifallah*¹, Christiane Grimm¹, Aysha Mohamed-Lafirdeen¹, Xiaoyu Lu², François
4 St-Pierre^{2,3,4}, Eirini Papagiakoumou^{1§}, and Valentina Emiliani^{1§}

5
6 ¹Institut de la Vision, Sorbonne Université, INSERM, CNRS, F-75012 Paris, France

7 ²Systems, Synthetic, and Physical Biology Program, Rice University, Houston, TX, USA

8 ³Department of Neuroscience and Department of Biochemistry and Molecular Biology, Houston, TX, USA

9 ⁴Department of Electrical and Computer Engineering, Rice University, Houston, TX, USA

10
11 *Equal contribution

12
13 §valentina.emiliani@inserm.fr

14 §eirini.papagiakoumou@inserm.fr

15
16 Keywords: Two-photon microscopy, voltage imaging, temporal focusing, optogenetics, computer-
17 generated holography

18 19 **Abstract**

20
21 Parallel light-sculpting methods have been used to perform scanless two-photon photostimulation of
22 multiple neurons simultaneously during all-optical neurophysiology experiments. We demonstrate that
23 scanless two-photon excitation also enables high-resolution, high-contrast, voltage imaging by efficiently
24 exciting fluorescence in a large fraction of the cellular soma. We present a thorough characterisation of
25 scanless two-photon voltage imaging using existing parallel approaches and lasers with different repetition
26 rates. We demonstrate voltage recordings of high frequency spike trains and sub-threshold depolarizations
27 in intact brain tissue from neurons expressing the soma-targeted genetically encoded voltage indicator
28 JEDI-2P-kv. Using a low repetition-rate laser, we perform recordings from up to ten neurons simultaneously.
29 Finally, by co-expressing JEDI-2P-kv and the channelrhodopsin ChroME-ST in neurons of hippocampal
30 organotypic slices, we perform single-beam, simultaneous, two-photon voltage imaging and
31 photostimulation. This enables in-situ validation of the precise number and timing of light evoked action
32 potentials and will pave the way for rapid and scalable identification of functional brain connections in intact
33 neural circuits.

34 Introduction

35 Deciphering the logic and syntax of neural computation is a central goal in neuroscience and requires
36 methods to record (read-out) and manipulate (write-in) the activity of individual neurons.
37 Electrophysiological methods have proven instrumental towards achieving this goal since they can read
38 and write neural activity with high fidelity. However, while extracellular probes can record from large
39 populations, they have limited spatial resolution and cannot excite or inhibit specific neurons. In contrast,
40 whole-cell patch-clamp methods can manipulate and record the electrical activity of targeted neurons but
41 are hard to achieve *in vivo* even for a handful of neurons simultaneously and are unsuitable for longitudinal
42 (chronic) studies. Furthermore, all electrophysiological methods have limited access to smaller cellular
43 compartments of neurons (such as axons, distal dendrites, spines and boutons). These limitations have
44 stimulated the development of a plethora of minimally invasive photonic approaches, combining advanced
45 optical methods with light-sensitive proteins, such as genetically encoded fluorescent indicators and
46 optogenetic actuators, for recording and manipulating neural activity, respectively¹⁻³.

47
48 In the nervous system, calcium ions regulate a broad range of processes and generate versatile intracellular
49 signals⁴. Since action potentials lead to a large elevation of intracellular calcium, which can last an order of
50 magnitude longer than the action potentials themselves⁵, the developments of synthetic⁶ and genetically
51 encoded⁷ fluorescent calcium indicators (GECIs) capable of reporting changes in intracellular calcium were
52 extremely important scientific breakthroughs. GECIs can be targeted to sub-cellular compartments and
53 specific cell types^{8,9}. Their long-term expression in intact tissues and organisms² enables the repeated
54 observation of individual cells. Calcium transients last significantly longer than the underlying voltage
55 fluctuations, facilitating the detection of neural activity, but also limiting the quantification of spike firing rate
56 and timing. Furthermore, GECIs are not well-suited for detecting sub-threshold voltage changes and
57 hyperpolarizations resulting from synaptic and neuromodulatory inputs¹⁰.

58
59 Voltage indicators, which generate optical signals whose magnitude varies as a function of membrane
60 potential, promise to address many of the aforementioned limitations of GECIs¹¹. Following the first optical
61 recordings of membrane potential with a synthetic dye¹², voltage-sensitive indicators have undergone
62 continual advancements, including improved synthetic dyes¹³, genetically encoded voltage indicators
63 (GEVIs) and hybrid GEVIs¹⁴. However, detecting voltage spikes with GEVIs requires millisecond-timescale
64 imaging, two orders of magnitude faster than generally required for GECIs. This technical challenge has
65 limited the broad adoption of GEVIs for population imaging with cellular resolution.

66
67 The majority of voltage imaging experiments have relied on widefield, one-photon (1P) illumination and
68 detection. The resulting mesoscopic observations of population activity have enabled investigation of the
69 functional organisation and dynamics of cell-type specific excitatory and inhibitory cortical circuits^{15,16}. The
70 lack of optical sectioning of 1P widefield microscopy has been overcome using sparse labelling strategies¹⁷

71 or sculpted illumination^{18–21}. However, these strategies are not suitable for multitarget voltage imaging in
72 densely labelled scattering samples with cellular resolution, such as mammalian in-vivo preparations.

73

74 In principle, the optical sectioning inherent to two-photon excitation can be used to overcome these
75 problems²², and two-photon laser scanning microscopy (2P-LSM) is commonly used to perform calcium
76 imaging in scattering tissue²³. However, the acquisition rate of conventional 2P-LSM is limited and
77 millisecond transients such as action potentials can only be detected by drastic reduction of the field of
78 view^{24–27}. As a result, several specialised scanning-based techniques have been developed to image neural
79 activity across larger areas at kilohertz rates^{28–35} and have yielded spectacular results, such as recording
80 the voltage dynamics of cortical neurons in layer 5 in awake behaving mice. However, these methods are
81 extremely technically demanding, have thus-far been limited to imaging a few cells simultaneously, and
82 have not yet been demonstrated to be compatible with two-photon optogenetics, as required for two-photon,
83 all-optical neurophysiology experiments.

84

85 Here, we propose an alternative approach for high-contrast, high-resolution, voltage imaging in densely
86 labelled samples that is compatible with simultaneous two-photon optogenetic stimulation. Our method
87 leverages existing scanless two-photon excitation approaches^{36–39} and the recently developed soma-
88 targeted GEVI JEDI-2P-kv⁴⁰. We demonstrate that, in combination with temporal focusing (TF)^{41–43}, the
89 three light-sculpting approaches commonly used for scanless two-photon photoactivation —Generalised
90 Phase Contrast (GPC)^{36,38}, low numerical aperture (NA) Gaussian beams (such as 3D-SHOT)^{39,44} and
91 Computer-Generated Holography (CGH)^{45,46}— enable voltage imaging in mammalian cells. By performing
92 simultaneous imaging and electrophysiology, we provide a thorough quantitative comparison of these
93 illumination modalities. Next, by viral expression of JEDI-2P-kv in mouse hippocampal organotypic slices,
94 we show that 2P-TF-GPC enables high spatiotemporal resolution voltage imaging of neural activity in
95 extremely densely labelled preparations. We further demonstrate the detection of high-frequency spike
96 trains and subthreshold membrane depolarizations with amplitudes on the order of excitatory postsynaptic
97 potentials (PSPs). Capitalising on the overlapping spectra of JEDI-2P-kv and the channelrhodopsin
98 ChroME-ST⁴⁴, we demonstrate simultaneous two-photon voltage imaging and photostimulation in multiple
99 cells. This approach enables *in-situ* characterisation of the light-induced spiking properties of a population
100 of neurons. Collectively, these results pave the way for studying neural function with two-photon all-optical
101 neurophysiology in highly-scattering, densely labelled preparations.

102 **Results**

103 **Scanless two-photon voltage imaging with sculpted, temporally focused excitation**

104 The optical setup (Figure 1a, Supplementary Figure 1 and Table S1) was comprised of two independent
105 excitation paths, one designed to generate temporally focused (TF) Generalized Phase Contrast (GPC)
106 patterns^{36,38} or low NA Gaussian spots (similar to 3D-SHOT³⁹), and the second for TF-Computer Generated
107 Holography (CGH)³⁷. These paths were combined prior to the microscope objective with a polarising beam
108 splitter. Each excitation path was designed to generate temporally focused spots with dimensions matching
109 the typical size of a neuronal soma (12 μm lateral full width at half maximum (FWHM) and ~ 9 μm axial
110 FWHM for all modalities (Figure 1b, c, Supplementary Note 2, Supplementary Figures 2-5)). The
111 fluorescence from 1 μm microspheres excited with a 12 μm GPC spot was recorded and found to have an
112 axial FWHM of 3.7 μm demonstrating sub-cellular axial resolution (Figure 1c, right panel). In all cases,
113 emitted fluorescence was detected by an sCMOS camera, effective pixel size 0.1625 μm . The nominal field
114 of excitation of each of the light sculpting approaches was 250 x 250 μm^2 ^{6,34,35}. However, the effective
115 imaging field of view was limited in one dimension by the number of sCMOS rows readout simultaneously
116 at a given acquisition rate (see Methods). The system was equipped with three different laser sources, two
117 high repetition rate oscillators (as commonly used for two-photon laser scanning microscopy; 80 MHz, 920
118 or 940 nm, 100 fs, 12.5 nJ and 50 nJ pulse energies) and a third low repetition rate, high pulse energy laser
119 (250 kHz, 940 nm, 100 fs, up to 2.5 μJ energy per pulse).

120 We compared the performance of three excitation modalities (2P-TF-GPC, 2P-TF-Gaussian and 2P-TF-
121 CGH) for scanless two-photon voltage imaging using a high repetition rate laser source, as typically used
122 for conventional 2P-LSM. We transiently expressed a recently developed, negative-going, voltage indicator
123 optimised for two-photon excitation (JEDI-2P-kv⁴⁰), in mammalian (CHO) cells (Figure 2a). We controlled
124 the membrane potential of individual cells using whole-cell patch-clamp electrophysiology and
125 simultaneously performed two-photon voltage imaging. We used three different protocols, hereafter named
126 1, 2 and 3 (Figure 2b), to test the feasibility of scanless two-photon voltage imaging and to assess the
127 advantages and disadvantages of each parallel approach.

128 Protocol 1 was used to quantify the voltage sensitivity of fluorescence of cells expressing JEDI-2P-kv. The
129 responses of patched cells to three 100 ms, 100 mV voltage steps were recorded at 100 Hz under
130 continuous illumination (power density: 0.88 mW μm^{-2} , 100 mW per cell) for 3 seconds. Voltage responses
131 were clearly observed as a decrease in fluorescence with 2P-TF-GPC, 2P-TF-Gaussian and 2P-TF-CGH
132 (Figure 2b, left panel). For most cells, we observed variability between the response amplitude measured
133 at different membrane locations. Since differences in voltage responsivity of the fluorescence originating
134 from different portions of the membrane were random, this is plausibly due to differences in plasma
135 membrane trafficking and protein folding.

136 All data acquired using protocol 1 (n = 41 cells) were pooled and used to establish and validate an analysis
137 pipeline capable of automatically identifying and segmenting neurons and of detrending the optical traces
138 (Supplementary Figure 6). Due to the similarities between the data obtained with scanless two-photon
139 voltage imaging and single photon voltage imaging with widefield detection, it was possible to develop an
140 analysis pipeline based on existing open-source packages. Compared with results obtained by calculating
141 the unweighted mean of all pixels within segmented cells, the regression-based pixel weighting
142 algorithm^{14,49-51} (Methods, Supplementary Note 3), which improved segmentation, was found to increase -
143 $\% \Delta F/F_0$ for all modalities (33.8 ± 9.5 vs. 43 ± 11.7 , mean \pm s.d., $p < 0.00001$, $n=41$, Supplementary Figure
144 7b), resulting in values in accordance with those previously reported⁴⁰. No significant difference in SNR
145 (signal amplitude divided by the standard deviation of the baseline signal) was found between the two
146 approaches (59.4 ± 30.2 vs. 59.6 ± 31.3 , $p = 0.9158$, $n=41$, Supplementary Figure 7c), a result of the fact
147 that the improved segmentation contained approximately half of the pixels of the initial segmentation (16263
148 ± 2180 vs. 8962 ± 2676 , $p < 0.00001$, $n=41$, Supplementary Figure 7d). However, the location of these
149 pixels coincided with the exterior cell membrane (Supplementary Figure 7d, inset), the most voltage-
150 sensitive, which compensated for the effective reduction in photon count. We found that the final traces
151 generated using the weighted pixel mask exhibited slightly more photobleaching than the traces generated
152 with the original segmentation (0.82 ± 0.02 vs. 0.80 ± 0.03 , $p < 0.00001$, $n=41$, Supplementary Figure 7e).
153 This is likely the result of two factors. Firstly, responsive pixels imaged with high contrast are more likely to
154 be retained in the second segmentation step. These pixels are those where the cellular equator coincided
155 with the focal plane, where the excitation power density (and presumably photobleaching) is highest.
156 Secondly, the voltage responsive fluorophores are more likely to be tethered to the membrane, less mobile
157 and hence more susceptible to photobleaching.

158 Having established the analysis pipeline, we then compared the three excitation modalities (Supplementary
159 Figure 8). 2P-TF-GPC, 2P-TF-Gaussian and 2P-TF-CGH were all found to be suitable for scanless two-
160 photon voltage imaging. Data obtained with 2P-TF-CGH exhibited the highest signal-to-noise ratio ($81.6 \pm$
161 35.3 , $n = 15$), almost double that of 2P-TF-GPC (48.5 ± 19.2 , $p = 0.00222$, $n = 17$) and 2P-TF-Gaussian
162 (43.9 ± 20.3 , $p = 0.00608$, $n = 9$). We hypothesised this was because the high spatial density of photons in
163 speckle grains results in more efficient two-photon excitation. This hypothesis was confirmed by simulations
164 (Supplementary Note 2, Supplementary Figure 5).

165
166 Since the high density of photons in speckles also increase the likelihood of non-linear photophysics (for
167 instance photobleaching⁵²), we designed and used a different protocol (Protocol 2) to investigate the extent
168 of these non-linear effects as a function of the excitation power density ($0.66 - 1.55 \text{ mW } \mu\text{m}^{-2}$ corresponding
169 to $75 - 175 \text{ mW}$ per cell). Protocol 2 consisted of three 100 ms, 100 mV voltage steps, 200 ms illumination
170 pulses centred on each voltage step, and 2.5 s inter-pulse intervals (Figure 2b, middle panel). For all
171 modalities, the baseline fluorescence (F_0) increased quadratically as a function of power density (Figure
172 2c, first panel), as expected with two-photon illumination and indicating that fluorescence excitation was not

173 saturated at any of the powers used. Furthermore, the SNR increased linearly as a function of power density
174 (Figure 2c, second panel, $R^2 = 0.999$ (2P-TF-GPC), $R^2 = 0.995$ (2P-TF-Gaussian), $R^2 = 0.998$ (2P-TF-
175 CGH)), confirming that experiments were performed in the shot-noise limited regime rather than being
176 limited by the read noise of the detector. On this basis, all SNR estimates stated hereafter were calculated
177 as $SNR = (-\Delta F/F_0) \sqrt{F_0}^{53}$.

178

179 The SNR of the responses to 100 mV steps (Protocol 2) was higher at all excitation power densities with
180 2P-TF-CGH than with 2P-TF-GPC or 2P-TF-Gaussian, (Figure 2c, second panel, Supplementary Figure
181 9a), though the 2P-TF-CGH fluorescent transients exhibited a systematically lower average $-\% \Delta F/F_0$ than
182 when using 2P-TF-GPC. This difference increased as a function of power density (Figure 2c, third panel,
183 Supplementary Figure 9b). Photostability, defined as the ratio between the integral of the baseline
184 fluorescent trace to $F_0 \cdot n_t$ where F_0 represents the fluorescence in the first frame and n_t the number of
185 baseline fluorescence timepoints (schematic diagram, Figure 2c, fourth panel, inset), decreased as a
186 function of excitation power in all cases (Figure 2c, fourth panel). No significant difference was observed
187 between the different modalities (Supplementary Figure 9c). Photorecovery, quantified as the ratio of
188 fluorescence after dark intervals to the original fluorescence (schematic diagram, Figure 2c, fourth panel,
189 inset), was over 97% following 2.5 s dark inter-pulse intervals when excited with 2P-TF-Gaussian and 2P-
190 TF-GPC, which is consistent with previous observations²⁸. In the case of 2P-TF-CGH, the photorecovery
191 decreased as a function of excitation power density and was lower than the other modalities (<95% for
192 power densities greater than $0.88 \text{ mW } \mu\text{m}^{-2}$ (100 mW per cell), $p=0.01$, Figure 2c, fifth panel, Supplementary
193 Figure 9d).

194

195 Finally, we used protocol 3 (Figure 2b, right panel) to assess the detection of short, action-potential like
196 transients with scanless two-photon voltage imaging. Cells were illuminated continuously for 500 ms (power
197 density: $1.33 \text{ mW } \mu\text{m}^{-2}$, corresponding to 150 mW per cell) and the fluorescence response to a 20 Hz train
198 of 10 rectangular pulses (100 mV amplitude, 3 ms duration) was recorded with a 1 kHz acquisition frequency
199 (see Methods). The transients recorded using 2P-TF-GPC, 2P-TF-Gaussian and 2P-TF-CGH, had $-\% \Delta F/F_0$
200 values of $45 \pm 14 \%$, $42 \pm 16 \%$ and $26 \pm 6 \%$ ($n = 8-11$) respectively (Supplementary Figure 10b). For all
201 modalities, the average SNR was greater than 11, demonstrating that action-potential-like signals can be
202 reliably detected in single trials with scanless two-photon voltage imaging. As per data presented in
203 supplementary figures 10c and d, the highest SNR data was acquired using 2P-TF-CGH (20.5 ± 6.2)
204 compared with 13.9 ± 3.6 (2P-TF-GPC) and 11.5 ± 4.1 (2P-TF-Gaussian), $n = 8-11$), at the cost of lower
205 photostability (0.86 ± 0.07 (2P-TF-CGH) versus 0.92 ± 0.08 (2P-TF-GPC) and 0.89 ± 0.12 (2P-TF-
206 Gaussian), $n = 8-11$).

207

208 Overall, these results confirm that 2P-TF-GPC, 2P-TF-Gaussian and 2P-TF-CGH can successfully be
209 applied to scanless two-photon voltage imaging, albeit with different advantages and limitations. Since the

210 SNR of data acquired using 2P-TF-CGH was significantly higher than for 2P-TF-Gaussian or 2P-TF-GPC,
211 we consider it the optimal modality for imaging large numbers of cells simultaneously, for short periods,
212 with a given incident power. For prolonged recordings (continuous illumination for hundreds of milliseconds
213 or more) of neurons labelled with JEDI-2P-kv, we would recommend 2P-TF-GPC or 2P-TF-Gaussian, since
214 we observed lower photobleaching and higher photorecovery with these methods than with 2P-TF-CGH.
215 Although no significant performance differences were found between 2P-TF-Gaussian and 2P-TF-GPC
216 (Figure 2c, Supplementary Figures 8 and 9), 2P-TF-Gaussian requires higher power at the laser output for
217 a given SNR. Specifically, uniform illumination of the somal membrane was achieved with 2P-TF-Gaussian
218 by expanding and subsequently cropping the beam (Supplementary Note 2, Supplementary Figure 4) and
219 thus was ~3 times less power-efficient than 2P-TF-GPC⁵⁴. However, it is perhaps the simplest approach to
220 implement, and hence a good solution given a sufficiently powerful laser source.

221

222 **Scanless voltage imaging of neural activity in hippocampal organotypic slices with two-photon,** 223 **temporally focused Generalised Phase Contrast**

224 We set out to identify the imaging conditions (specifically the power densities and acquisition rates) required
225 to observe neural activity ranging from high-frequency spike trains to sub-threshold depolarizations in
226 densely labelled samples. We also aimed to determine whether the necessary imaging conditions perturb
227 neural activity or otherwise impact cellular physiology. We performed simultaneous 2P-TF-GPC imaging
228 and whole cell-patch clamp recordings of granule cells located in the dentate gyrus (DG) of organotypic
229 slices bulk-transduced with JEDI-2P-kv (see Methods). Expression of JEDI-2P-kv in the granule cells of the
230 DG was well localised to the plasma membrane, with no evidence of intracellular aggregation (Figure 3a).
231 Even though granule cells are extremely closely packed in DG, due to the optical sectioning conferred by
232 temporally focused, targeted illumination, we were able to image individual neurons with high-contrast and
233 high-resolution in this challenging preparation (Figure 3b).

234 Using protocol 1, we confirmed we could detect 100 mV depolarizations in densely labelled, scattering
235 organotypic slices with comparable $-\% \Delta F/F_0$ (43 ± 8) to that obtained in CHO cells (51 ± 11) ($n > 15$ cells,
236 accounting for differences in the resting potential between neurons and CHO cells, Supplementary Figures
237 11 and 12). No significant difference was observed in SNR (69 ± 25 (CHO), 50 ± 30 (organotypic slices), n
238 > 15 cells, Supplementary Figure 12e) or photostability between results obtained in hippocampal
239 organotypic slices and CHO cells. The effective lateral and axial resolution of the scanless two-photon
240 imaging system, quantified as the relative $\Delta F/F_0$ of an electrically evoked spike as a function of the distance
241 between the excitation spot and the soma, was found to be approximately isotropic and of similar
242 dimensions to the neuronal soma ($14 \mu\text{m}$ lateral and $13 \mu\text{m}$ axial FWHM, Supplementary Figure 12h),
243 confirming the cellular resolution of scanless two-photon voltage imaging.

244 Next, we recorded the fluorescence from patched cells while 50 action potentials (APs) were evoked
245 electrically by injection of current (700 - 900 pA, 2 ms) into the soma at a rate of 1 Hz. Electrically evoked
246 APs were imaged with 3 different acquisition rates: 500 Hz, 750 Hz, and 1 kHz (corresponding to per-frame
247 exposure times of 2, 1.33 and 1 ms respectively) as previously used for 1P widefield voltage imaging²¹. In
248 all conditions, individual APs could clearly be identified from single trials in the raw fluorescence traces
249 (representative traces for single cells plotted in Figure 3c, power density: 1.11 mW μm^{-2} , corresponding to
250 125 mW per cell). Putative APs were identified by template matching, based on the most prominent peaks
251 originally identified in each fluorescence trace⁵⁰. The 1 kHz recordings exhibited a higher $-\% \Delta F/F_0$ than 500
252 Hz recordings across all powers (30.5 ± 2.2 vs 25.7 ± 1.2 , $n > 5$ cells, Figure 3d). However, consistent with
253 previous reports¹⁷, higher SNR was achieved with 500 Hz recordings than for 1 kHz (for example for 0.66
254 mW μm^{-2} (75 mW per cell): 14.2 ± 0.3 vs 11.9 ± 0.3 , Figure 3d), because the increase in the number of
255 photons collected per action potential more than compensated for the reduced $-\% \Delta F/F_0$.

256 Having established that it was possible to record APs with high SNR in single trials at different acquisition
257 rates, we next tested whether we could also monitor individual spikes within high-frequency trains of action
258 potentials (such as bursts) under these conditions. We observed that an acquisition rate of 500 Hz was
259 sufficient to track individual APs in trains with frequencies up to 100 Hz (Figure 3e, Supplementary Figure
260 13) and using power densities as low as 0.66 mW μm^{-2} (75 mW per cell). As a result of increased SNR
261 recordings with lower acquisition rates, at low power densities, the detection probability (fraction of correctly
262 identified APs) was higher (Figure 3f). Note that the difference in SNR between results presented in Figure
263 3d and Figure 3f is the result of using different cameras and different excitation wavelengths, as specified
264 in the Methods and Supplementary Tables 1 and 2. However, an acquisition rate of 500 Hz was insufficient
265 for robustly tracking spikes in 125 Hz trains due to a reduction in $-\% \Delta F/F_0$ (Supplementary Figure 13b),
266 which led to a deterioration in detection probability and fluorescence response compared with the data
267 acquired at 1 kHz at power densities ≥ 0.66 mW μm^{-2} (corresponding to 75 mW per cell, Figure 3f,
268 Supplementary Figure 13). For all power densities > 0.66 mW μm^{-2} (75 mW per cell) sub-millisecond
269 precision of AP timing estimation was obtained, as measured with respect to the electrophysiology trace
270 (Figure 3f).

271 We next examined whether these conditions (power density: 1.11 mW μm^{-2} , corresponding to 125 mW per
272 cell, 1 kHz acquisition rate) were also suitable for imaging sub-threshold changes in membrane potential.
273 To emulate excitatory PSPs, patched cells were clamped to -75 mV, while the membrane potential was
274 varied in 0.5 mV steps from 0 to 2.5 mV for 20 ms. This protocol was repeated 50 times. Since it was not
275 possible to detect these transients from individual recordings (Figure 4a, b, $n=6$), we averaged data from
276 different trials to improve SNR. Averaging data from 25 repeats was sufficient to stabilise the magnitude of
277 the fluorescence transient ($-\% \Delta F/F_0$) for a given depolarization (Figure 4a, c) and to increase the SNR
278 above 1 for all depolarizations larger than 0.5 mV (Figure 4d).

279 Next, we tested the capability of scanless two-photon voltage imaging to record spontaneous network
280 activity, a fundamental feature of developing neural circuits⁵⁴. We performed simultaneous
281 electrophysiological (whole cell patch clamp, (current clamp)) and fluorescence recordings (2P-TF-GPC,
282 power density: $1.33 \text{ mW } \mu\text{m}^{-2}$ (150 mW per cell), 1 kHz acquisition rate) of spontaneous activity from
283 neurons in hippocampal organotypic slices which exhibited a range of different resting potentials ($n > 10$
284 cells; 5 slices). We were able to observe several hallmarks of spontaneously generated activity, large slow
285 depolarizations, bursts of action potentials, rhythmic sub-threshold depolarizations and hyperpolarizations
286 (Figure 5 and Supplementary Figure 14). These results confirmed the capability of scanless two-photon
287 voltage imaging for high temporal precision, single trial recordings of action potentials and sub-threshold
288 events, even though the sensitivity curve of JEDI-2P-kv is not optimized for sub-threshold recordings.
289 Collectively, the results presented in Figures 3-5 parameterize the necessary imaging conditions required
290 to detect neural activity with sufficient SNR using scanless two-photon voltage imaging.

291 To test the robustness of our approach for long-term recordings, we repeated the same protocol (2P-TF-
292 GPC, 30 s continuous illumination, $1.33 \text{ mW } \mu\text{m}^{-2}$ (150 mW per cell), 1 kHz acquisition rate), for a maximum
293 recording time of 20 minutes. Due to limitations of the prototype experimental configuration (primarily data
294 transfer rates), there was a dark period (<10 seconds) between consecutive acquisitions. To increase the
295 duty cycle of the recordings, we reduced the acquisition speed to 500 Hz which enabled us to perform
296 longer continuous recordings with a shorter dark period of <5 seconds (2P-TF-GPC, 1 min continuous
297 illumination, $1.33 \text{ mW } \mu\text{m}^{-2}$ (150 mW per cell), 500 Hz acquisition rate). As indicated by the data presented
298 in Supplementary Figure 15, we were able to record spontaneous activity from single neurons for a
299 maximum recording time of 20 minutes without a significant decrease in SNR (Supplementary Figure 15b).
300 The imaging period was primarily limited by axial sample drift which decreased the SNR (data not shown),
301 but could be overcome in future experiments with a tandem construct containing the voltage indicator and
302 a spectrally shifted, fluorescent reporter used to track the sample drift and to dynamically update the co-
303 ordinates of the multiplexed spots.

304 Having established the conditions necessary to observe neural activity ranging from high-frequency trains
305 of action potentials to sub-threshold membrane potential depolarizations, we next investigated whether
306 such imaging conditions induced physiological perturbations. There are two main sources of light-induced
307 perturbations. The first is heating, due to linear absorption of the infrared light (mostly by water), which has
308 been reported to affect ion channel conductances⁴⁵ and action potential waveforms⁴⁶. The second is non-
309 linear photodamage, due to higher order light-matter interactions which occur because of high
310 instantaneous photon density in the focal volume and can ultimately induce apoptosis and cell ablation<sup>47-
311 49</sup>. We performed experiments (10 ms strobed illumination, 50 cycles, 1 Hz, total illumination time 500 ms,
312 >15 cells per region, targeted sequentially: identical to the protocol used to detect APs (Figure 3b-c)) at
313 power densities we found necessary to observe neural activity with sufficient SNR and above ($0.66 - 1.55$
314 $\text{mW } \mu\text{m}^{-2}$, corresponding to 75 – 175 mW per cell). Following these experiments, we used

315 immunohistochemistry to detect heat-shock proteins (anti-HSP70/72 immunostaining) and activation of
316 apoptotic pathways (anti-activated-Caspase-3 immunostaining). Fixed slices were imaged using confocal
317 microscopy. No difference in fluorescence intensity was observed between any of the illumination powers
318 used and the control slices (not illuminated) in the case of Caspase-3 (Supplementary Figure 16a). In
319 contrast, we observed that levels of anti-HSP increased as a function of excitation power above 1.1 mW
320 μm^{-2} (125 mW per cell), which indicates that the physiological damage induced by the high repetition rate
321 laser sources, is predominantly heating. Since the damage threshold of 1.1 mW μm^{-2} (125 mW per cell)
322 identified using immunohistochemistry is an upper bound, we also investigated whether there was any light
323 induced changes in the electrical properties of neurons using electrophysiology. We did not observe any
324 light-induced changes in action potential amplitude or width at any of the tested powers (Supplementary
325 Figure 16b), however we found that the latency of action potential firing slightly increased at all powers
326 tested (0.1 ms, Supplementary Figure 16b). This effect was observed 15 seconds before a similar increase
327 in latency was seen in control experiments (Supplementary figure 16b). Whilst a 10 percent change is not
328 huge, the immunohistochemistry and electrophysiology results imply a laser-induced perturbation of
329 physiology for powers > 125 mW per cell.

330 **Scanless two-photon voltage imaging of multiple targets with low repetition rate lasers**

331 To test the capability of multiplexed 2P-TF-GPC to image multiple neurons simultaneously we used a
332 custom low-repetition rate source (940 nm, pulse duration 100 fs, repetition rate 250 kHz, 600 mW average
333 output power). Low-repetition rate sources, used for two-photon optogenetics, can provide higher peak
334 energies and lower average power, hence potentially minimize photoinduced thermal effects and scale up
335 the number of neurons that can be imaged simultaneously. Low-repetition rate lasers are particularly well
336 suited for techniques with long times, such as scanless two-photon imaging. We found that using the low
337 repetition rate laser, action potentials could be detected in single trials with power densities as small as
338 0.01 mW μm^{-2} (1.5 mW per cell, Supplementary Figure 17). In contrast to the results obtained using the
339 high repetition rate source (80 MHz, previous section), no changes in action potential properties were
340 detected at any of the tested powers (Supplementary Figure 17). Immunohistochemistry targeted against
341 HSP70/72 and activated-Caspase-3 (Supplementary Figure 17) did not reveal thermal or non-linear
342 damage at power densities below 0.09 mW μm^{-2} (10 mW per cell) using 2P-TF-CGH, two-fold higher than
343 the maximum powers we found typically necessary to image neural activity. Extrapolating from the results
344 related to photobleaching and photostability obtained in CHO cells, we anticipate higher non-linear damage
345 thresholds for 2P-TF-GPC and 2P-TF-Gaussian.

346 As a result of the increased energy per pulse of the low-repetition rate source, we were able to increase
347 the number of neurons imaged simultaneously without exceeding the power damage threshold. For
348 example, we recorded spontaneous activity in up to 8 neurons in the dentate gyrus of hippocampal
349 organotypic slices simultaneously (2P-TF-GPC, power densities: 0.04 – 0.08 mW μm^{-2} (5 – 9 mW per cell,
350 total power < 75 mW), Figure 6, Supplementary Figure 18). The sub-threshold activity of most neurons was

351 found to be highly synchronized, a characteristic feature of the immature hippocampus⁵⁴. Control traces
352 recorded adjacent to targeted neurons confirmed that this was not an artefact due to crosstalk. We were
353 able to combine data from separate acquisitions to perform voltage imaging throughout a large region (200
354 x 150 μm^2) as demonstrated in Figure 6. Since this data was acquired on a prototype system, the period
355 between sequential acquisitions was on the order of seconds. However, by optimizing the acquisition
356 pipeline, the period between sequential acquisitions could feasibly be reduced to milliseconds to enable
357 scanless two-photon voltage imaging of populations of neurons.

358 The number of achievable targets per acquisition and/or the imaging depth could be further increased, as
359 demonstrated for two-photon photostimulation of multiple cells⁵⁵ using high-power, low repetition rate,
360 industrial light sources such as Ytterbium-doped fibre lasers which can provide much higher output powers
361 (tens of Watts), and comparable pulse energies to the 940 nm source used in this work. These lasers are
362 commonly fixed wavelength sources (1030 – 1040 nm), which means that they are not typically compatible
363 with GFP-based fluorescent indicators. However, since the excitation spectrum of JEDI-2P-kv is slightly
364 red-shifted as compared with previous GFP-based voltage indicators⁴⁰, we tested whether it was possible
365 to record neural activity using scanless two-photon voltage imaging with 1030 nm excitation. We repeated
366 protocol 2 (see above) in CHO cells and imaged electrically evoked action potentials and spontaneous
367 activity in sparsely labelled hippocampal organotypic slices (Supplementary Figure 19).

368 **Scanless two-photon voltage imaging and photostimulation of multiple targets with a single beam**

369 Next, we performed simultaneous two-photon voltage imaging and photostimulation of neurons co-
370 expressing JEDI-2P-kv and a soma-targeted channelrhodopsin. ChroME-ST and JEDI-2P-kv were co-
371 expressed in the dentate gyrus of hippocampal organotypic slices by bulk transduction of two Adeno-
372 Associated Virus (AAV) vectors (Figure 7a). We characterised the photophysical properties of ChroME-ST
373 excited using the low-repetition rate laser using whole cell patch clamp electrophysiology (voltage-clamp).
374 ChroME-ST mediated photocurrents in CHO cells saturated at 0.02 $\text{mW } \mu\text{m}^{-2}$ (2.5 mW per cell)
375 (Supplementary Figure 20, n=4). In hippocampal organotypic slices, power densities between 0.02 and
376 0.04 $\text{mW } \mu\text{m}^{-2}$ (2.5 - 5 mW per cell) generated sufficiently large photocurrents to reliably evoke APs with
377 short (< 5 ms) latency and sub-millisecond jitter (Supplementary Figure 20, n=7).

378 We performed simultaneous photostimulation, imaging and whole-cell patch clamp recordings on neurons
379 co-expressing ChroME-ST and JEDI-2P-kv and confirmed that optically evoked action potentials could be
380 detected in voltage imaging recordings (Figure 7b). We next performed an all-optical characterisation of
381 ChroME-ST. By modifying the power, duration and frequency of the illumination, we explored the joint-
382 parameter space of imaging and stimulation conditions to optimize the probability of optically evoking and
383 recording action potentials (Figure 7c). Unlike in neurons exclusively expressing JEDI-2P-kv, at power
384 densities below 0.02 $\text{mW } \mu\text{m}^{-2}$ (2.5 mW per cell), the SNR of action potentials from single trials did not
385 exceed the SNR threshold and hence could not be detected optically (Figure 7c), although
386 electrophysiological recordings performed simultaneously indicated that the probability of optically evoking

387 an AP was greater than 75% (Supplementary Figure 20b). We attribute the reduction in SNR to a reduction
388 in the expression efficiency of JEDI-2P-kv as a result of co-expressing a voltage indicator and
389 channelrhodopsin, which results in a difference between the optical and electrophysiological results.
390 However, for power densities above $0.02 \text{ mW } \mu\text{m}^{-2}$ (2.5 mW per cell), we were able to detect action
391 potentials in single trials and measured similar latencies to those obtained using whole-cell patch clamp
392 recordings ($4.3 \pm 0.2 \text{ ms}$, mean \pm s.e.m.) and jitter on the order of a millisecond (Supplementary Figure
393 20c-d).

394 The action potential probability decreased as a function of stimulation frequency, feasibly a result of
395 channelrhodopsin desensitization at the saturating powers used, although in some cases it was possible to
396 stimulate and image action potentials at 50 Hz (Figure 7c, right panel). Based on this characterisation, we
397 determined that the optimal photostimulation and imaging parameters to robustly optically evoke and detect
398 action potentials were a frequency of 5 Hz and 15 ms photoactivation pulses. The extended illumination
399 time relative to typical photostimulation protocols was necessary for having sufficient baseline to calculate
400 $-\% \Delta F / F_0$ and to robustly detect optically evoked action potentials. Results obtained for these parameters
401 are summarized for 27 cells in the raster plot in Figure 7d with representative fluorescence traces of optically
402 evoked APs shown in Figure 7e. For each cell, the power density was increased until a spike was detected
403 optically in at least one of five repeats. The final set of power densities used was between 0.02 and 0.08
404 $\text{mW } \mu\text{m}^{-2}$ (2.5 and 9 mW per cell), below the power threshold found to induce physiological perturbations
405 (see above). The average $-\% \Delta F / F_0$ of optically evoked action potentials was found to be $20 \pm 8 \%$ ($n=33$;
406 Figure 7f), consistent with results obtained for electrically evoked action potentials (Figures 3d and f).

407 Next, we extended the unique capability of our approach of scanless two-photon voltage imaging to perform
408 simultaneous two-photon photostimulation and imaging of multiple cells (Figure 8). In each experimental
409 session, we first sequentially targeted cells that were expressing one or both constructs to quantify the
410 probability of false positives (Figure 8a-c). We detected an increase in fluorescence when targeting cells
411 only expressing ChroME-ST, due to excitation and detection of the nuclear-targeted fluorophore. No action
412 potentials were identified in cells that were not co-expressing the two constructs but were detected optically
413 in approximately fifty percent of co-expressing cells. We then simultaneously stimulated and imaged the
414 same group of cells (Figure 8d) with no deterioration of SNR or $-\% \Delta F / F_0$ of evoked and imaged action
415 potentials (Figure 8d) and were able to determine the number and timing of action potentials evoked, and
416 identify failures, during the stimulation period in multiple cells simultaneously (Figure 8e).

417 These results demonstrate that simultaneous, scanless two-photon voltage imaging and photostimulation
418 can be performed in multiple cells simultaneously using high-energy, low-repetition rate lasers, using
419 powers well-below the damage threshold.

420 Discussion

421 In this work, we introduced scanless two-photon voltage imaging and performed high-contrast, high-
422 resolution voltage imaging of single and multiple neurons expressing the newly developed GEVI JEDI-2P-
423 kv. Due to the axial confinement conferred by temporal focusing we were able to perform high-contrast two-
424 photon voltage imaging in densely labelled intact brain slices.

425 We performed a thorough characterisation of three, temporally focused, parallel excitation modalities (2P-
426 TF-Gaussian, 2P-TF-GPC and 2P-TF-CGH) for scanless two-photon voltage imaging. A strong advantage
427 of 2P-TF-Gaussian illumination (similarly to 3D-SHOT) is that it is the easiest and most cost-effective
428 approach to implement. 2P-TF-Gaussian beams have been used for volumetric Calcium imaging^{56,57}.
429 However, it is the least photon-efficient approach. Conversely, the photon-dense speckle grains in 2P-TF-
430 CGH spots result in efficient two-photon excitation and hence the highest SNR. In the case of limited power
431 budget, 2P-TF-CGH is thus the optimal modality for scanless multitarget voltage imaging. However, since
432 we observed higher photorecovery with 2P-TF-GPC and 2P-TF-Gaussian, these modalities are preferred
433 for prolonged (continuous illumination for hundreds of milliseconds or more) recordings such as imaging
434 spontaneous activity. Looking ahead, one of the primary advantages of 2P-TF-GPC is the capability of
435 sculpting well-defined lateral shapes³⁶ in order to target the most responsive regions of the cell membrane.
436 In contrast with existing two-photon voltage imaging approaches, the high lateral resolution (0.1625 μm
437 pixel size) of the experimental system presented in this manuscript would also be capable of sculpted,
438 scanless two-photon voltage imaging of thin subcellular processes.

439 We used 2P-TF-GPC to demonstrate many of the theorized advantages of imaging neural activity with
440 GEVIs by imaging action potentials (single-trial), subthreshold depolarizations and resolving single action
441 potentials in high-frequency spike trains up to 125 Hz. We performed simultaneous imaging and
442 electrophysiology to comprehensively characterize the performance of, and optimize, scanless two-photon
443 voltage imaging with the genetically encoded indicator JEDI-2P-kv. Consistent with previous reports³⁰, we
444 found that it was generally possible to reduce the imaging speed down to 500 Hz (and consequently the
445 required power) without a critical loss in the ability to determine the number and timing of action potentials.
446 However, these imaging speeds reduce the accuracy of action potential detection for spike trains with
447 frequencies > 100 Hz. The optimal imaging conditions will also depend on the characteristics of the specific
448 GEVI used. In principle, a major advantage of voltage versus calcium imaging in neuroscience is the ability
449 to detect sub-threshold changes in somatic membrane potential. In our current configuration, we found that
450 imaging small sub-threshold signals required averaging data from up to 25 individual trials to reach a SNR
451 above 1 for depolarizations larger than 0.5 mV. Whilst these findings highlight the challenges of detecting
452 subthreshold unitary PSPs (< 2.5 mV) *in vivo* with current state-of-the-art GEVIs under two-photon
453 excitation, they also indicate that such experiments ought to be possible using GEVIs optimized for sub-
454 threshold voltage detection.

455 Since the current implementation of scanless two-photon voltage imaging requires continuous illumination,
456 we carefully investigated whether the illumination conditions required to observe different aspects of neural
457 activity induced any observable physiological perturbations. We found that single cells could be imaged
458 using 100 fs, 80 MHz sources, at lower average powers than those commonly used for existing kilohertz
459 scanning microscopes applied to two-photon voltage imaging^{28,58,59} and did not observe any changes in AP
460 properties at these powers. However, we found that the latency of electrically induced APs was increased
461 slightly at all powers tested, and irreversible thermal damage was revealed with 2P-TF-CGH at the highest
462 powers tested using immunohistochemistry. In contrast, Caspase-3 staining did not reveal any non-linear
463 damage at the investigated powers. In fact, we found that one of the biggest impediments to long-term
464 voltage imaging was sample drift, a problem we imagine will be significantly more severe for scanless two-
465 photon imaging during future *in-vivo* experiments. To overcome this problem, we plan to use a tandem
466 construct containing the voltage indicator and a nuclear targeted, spectrally shifted, fluorescent reporter in
467 order to track the sample drift and to dynamically update the co-ordinates of the multiplexed spots. Use of
468 such a construct would also allow segmentation of the field of view and automated estimation of neuron
469 location, which also ought to increase the accuracy of spot position relative to the somal membrane.

470 We also demonstrated that scanless two-photon voltage imaging could be performed with a much lower
471 effective repetition rate (250 kHz) than used with existing kilohertz scanning microscopes. Even with this
472 low-repetition rate laser, fluorescence was excited with more than 50x the number of pulses per voxel than
473 for the scanning approaches. As a result, scanless two-photon voltage imaging is much more robust to
474 fluctuations in output laser power than the scanning approaches. We demonstrated AP detection in single
475 trials using 15-30 times lower average power than required using the high-repetition rate laser. Under these
476 conditions, we did not find any histological evidence of thermal stress or physiological perturbations with
477 whole-cell patch clamp recordings. As demonstrated in the case of two-photon optogenetics⁵⁵, the major
478 advantage of low-repetition rate lasers is that multiple targets can be illuminated simultaneously, whilst the
479 average power delivered to the sample is kept below the thermal damage threshold, and much lower than
480 the average powers used for existing kilohertz scanning microscopes. Specifically, in this work we were
481 able to perform simultaneous two-photon voltage imaging of spontaneous activity in multiple neurons (up
482 to 8) using a 100 fs, 250 kHz, 940 nm laser source (with between 200 - 600 mW exit power, corresponding
483 to a maximum average power of 60 mW at the sample). In order to increase the number of target cells, it
484 would be necessary to replace the laser source used in our experiments with a higher-power, low-repetition
485 rate industrial light source such as existing Ytterbium-doped fibre lasers (1030 nm, > 10 W output power).
486 In this work, we demonstrated that electrically evoked action potentials and spontaneous activity in
487 hippocampal organotypic slices could be recorded by exciting JEDI-2P-kv at 1030 nm. Based on the results
488 presented in this manuscript, with a 1030 nm Ytterbium-doped fibre source it would be feasible to record
489 the voltage of 40 cells simultaneously (5 mW per cell) using the existing configuration for scanless two-
490 photon voltage imaging, whilst remaining below the damage threshold (200 mW total average power).

491 The use of an SLM for holographic light multiplexing of the temporally focused, sculpted light resulted in a
492 nominal FOV of $250 \times 250 \mu\text{m}^2$. However, the effective FOV used for individual high-speed voltage imaging
493 recordings was reduced in one dimension due to the maximum number of rows of pixels that could be read
494 out at a given acquisition rate. We demonstrated that it was possible to perform voltage imaging throughout
495 the $250 \times 250 \mu\text{m}^2$ area and to combine data in post-processing, although this was not optimized on our
496 prototype system, and increasing the lateral field of view is one of the most urgent future avenues of
497 development. The field of view of scanless two-photon voltage imaging could be trivially increased by
498 reducing the magnification of the detection axis, although this would not be suitable for all experiments.
499 Furthermore, the sCMOS could be replaced with a detector capable of higher (full frame) readout speeds.
500 A primary motivation behind the development of holographic light multiplexing was to enable multitarget
501 photostimulation at axially distinct planes^{43,60,61}. Although our system is also capable of targeting neurons
502 in three-dimensions, we can currently only perform high-contrast imaging of a single plane. Performing
503 scanless activity recordings from multiple planes simultaneously would require increasing the depth of field
504 of the detection axis. For a very small number of discrete planes, this would be feasible using existing
505 approaches, such as remote focusing^{62,63}. More generally, camera-based volumetric voltage imaging will
506 require the implementation of computational imaging approaches, such as variants of light-field microscopy,
507 which have already been applied to imaging in scattering tissue⁶⁴.

508 All experiments in this study were performed at relatively superficial depths ($<50 \mu\text{m}$) in scattering tissue
509 where the expression pattern of JEDI-2P-kv was confined due to the approach used for viral delivery (bulk
510 transduction). The next step will be to monitor the membrane potential of multiple neurons simultaneously
511 *in-vivo*. It has already been demonstrated that temporal focusing preserves the profile and axial
512 confinement of sculpted light up to $500 \mu\text{m}$ in scattering tissue for the three excitation modalities used in
513 this work^{38,45}, and camera detection has also been used to perform functional imaging with multi-spot
514 excitation at depths up to $300 \mu\text{m}$ *in-vivo*^{65,66}. Hence it ought to be possible to perform scanless two-photon
515 voltage imaging in the upper cortical layer. Reaching deeper brain structures could be achieved by
516 combining camera detection with excitation through graded index lenses (GRIN) lenses^{67,68} or via emerging
517 computation approaches capable of overcoming scattering-induced ambiguity and of de-mixing the
518 fluorescent transients emanating from different sources⁶⁹.

519 We combined two-photon voltage imaging and optogenetics for the first time in proof-of-principle all-optical
520 neurophysiology experiments. We capitalized on the overlapping excitation spectra of JEDI-2P-kv and the
521 channelrhodopsin Chrome-ST to simultaneously evoke and record APs using a single beam. This approach
522 could be incorporated into all-optical experiments to dynamically tune the incident power necessary for
523 photostimulation and obtain the desired actuation on each of the targeted neurons *in situ*. In contrast to
524 approaches relying on inferring neural activity from GCaMP fluorescence⁷⁰, we demonstrated that voltage
525 imaging provides a direct readout of the precise number and timing of optically-evoked action potentials
526 with single spike precision at high spiking rates. The single beam approach to optically induce and read out

527 neuronal activity will also be a major addition in connectivity mapping to non-invasively confirm the
528 successful optical induction of an action potential in the potential pre-synaptic cell population. We
529 demonstrated that scanless two-photon imaging can be performed with any of the existing modalities used
530 for parallel two-photon photostimulation. As seen in our all-optical recordings (Figure 7d), the excitability of
531 the targeted cells can vary between cells and over time, advising a confirmation of the pre-synaptic spike
532 in each instance. In contrast to current connectivity mapping approaches, which do not confirm pre-synaptic
533 spiking⁷¹ or use GECIs⁷⁰, an approach using a voltage indicator would additionally reveal the precise timing
534 of the pre-synaptic spike, which would facilitate correlation of the post-synaptic response and discrimination
535 from noise. We anticipate that improved stoichiometric co-expression of the GEVI and the
536 channelrhodopsin, possibly using a fusion-construct for tandem expression where they are covalently
537 coupled, would facilitate the adoption of this approach.

538 The development of spectrally orthogonal voltage indicators and excitatory channelrhodopsins would
539 facilitate the next-generation all-optical neurophysiology experiments. For example, it would be possible to
540 record sensory-evoked activity patterns using voltage imaging, replay this activity using optogenetic
541 stimulation and, also tune the excitation parameters in order to explore the logic and syntax of neural
542 computation. Furthermore, this configuration would enable all-optical connectivity experiments whereby
543 putative presynaptic neurons are stimulated optogenetically and sub-threshold post-synaptic responses are
544 recorded optically. However, performing crosstalk-free all-optical neurophysiology experiments based on
545 two-photon excitation is not trivial since the majority of two-photon compatible voltage indicators are
546 optimally excited between 920 and 980 nm, a region of the electromagnetic spectrum where all commonly
547 used channelrhodopsin variants are persistently activated⁷². While all-optical experiments with calcium
548 indicators have been reported, similar results with GEVIs are more challenging due to the higher average
549 powers required for high-SNR millisecond-timescale voltage imaging. The development of performant red-
550 shifted genetically encoded voltage indicators, which could be combined with spectrally orthogonal blue-
551 shifted channelrhodopsins, will remove these remaining challenges and fill an important gap in the
552 optogenetic toolbox.

553 We anticipate that the description and thorough characterisation of scanless two-photon voltage imaging
554 presented in this manuscript will motivate its application to deciphering the logic and syntax of neural
555 circuits.

556

557 **Methods**

558 **Experimental setup for performing two-photon voltage imaging with temporally focused, sculpted** 559 **light**

560 All two-photon voltage imaging presented in this manuscript was performed using the experimental setup
561 presented in Supplementary Figure 1. In the schematic diagram, all reflective spatial light modulators
562 (SLMs) are shown as transmissive for illustrative purposes. Path 1 was used to generate temporally
563 focused, multiplexed, GPC (12 μm FWHM, 2PE) or low NA, apertured, Gaussian beams (12 μm FWHM,
564 2PE) respectively (upper path, Supplementary Figure 1). Path 2 (lower path, Supplementary Figure 1) was
565 used to generate temporally focused holographic disks (12 μm FWHM, 2PE). Three different laser sources
566 were used to acquire all data presented, referred to as Lasers A, B and C respectively throughout the
567 manuscript. The specific source used to acquire each dataset is specified in each case and all experimental
568 configurations used to acquire the data presented in each figure are summarised in Supplementary Tables
569 1 and 2. Laser A refers to a tuneable femtosecond source (Coherent Discovery, 80 MHz, 100 fs) tuned to
570 920, 940 or 1030 nm (as specified). Laser B refers to a femtosecond source with a fixed wavelength output
571 (Spark Alcor, 4 W, 80 MHz, 100 fs, 920 nm). Laser C refers to a custom OPA pumped by an amplified laser,
572 also with fixed wavelength output (Amplitude Satsuma Niji, 0.2 - 0.6 W, 250 kHz, 100 fs, 940 nm). By virtue
573 of the removable mirrors indicated in Supplementary Figure 1, light from each of the lasers could be directed
574 through path 1 or path 2 during a given experiment as indicated by the dashed lines in Supplementary
575 Figure 1. In all cases, the average laser power at the sample plane was controlled using a half-wave plate
576 (Thorlabs, WPHSM05-980) mounted on a motorised rotation mount (Thorlabs, PRM1Z8) in combination
577 with a polarising beam splitter (PBS), (Thorlabs, CCM1-PBS253/M). Prior to each experiment, the efficiency
578 of each path was measured. The power at the sample plane was recorded using a handheld power meter
579 (Thorlabs, S121C) and the power of the s-polarised light exiting the PBS at each laser output was measured
580 with a second power meter (Ophir, 30(150) A-BB-18, Nova II). The power of the s-polarised beam was
581 monitored continuously during experiments and used to update the rotation of the half-wave plate to deliver
582 the desired power at the sample plane during a given acquisition (calculated using the experimentally
583 measured efficiency of each path). All half-wave plates were externally triggered prior to each acquisition.
584 The output of lasers A and B was modulated by a mechanical shutter (Thorlabs, SH05R/M) or using a high-
585 speed modulator (Thorlabs, OM6NH/M) whereas the output of laser C was gated directly. In all cases the
586 external trigger was a TTL signal generated by pCLAMP (Molecular Devices, Sunnyvale, CA) controlling
587 an acquisition system (Molecular Devices, Axon Digidata 1550B).

588 In path 1, a telescope formed of two lenses (L1, $f = 80$ mm, (Thorlabs, AC508-80-B) and L2, $f = 300$ mm,
589 (Thorlabs, AC508-300-B), for GPC and L1, $f = 80$ mm, (Thorlabs, AC508-80-B) and L2, $f = 200$ mm,
590 (Thorlabs, AC508-200-B) for low-NA Gaussian illumination) was used to expand and project the beam onto
591 a spatial light modulator (SLM1), (Hamamatsu, LCOS 10468-07, 600×800 pixels, $20 \mu\text{m}$ pitch). In the case
592 of GPC, SLM1 was used to apply a π phase shift to the portion of the beam overlapping with the circular

593 spot and a phase shift of zero elsewhere. The modulated beam was Fourier transformed by L3, $f = 400$
594 mm, (Thorlabs, AC508-400-B), resulting in a spatial displacement between the low and high spatial
595 frequency components of the field in the Fourier plane. The low spatial frequency components were
596 selectively phase shifted by π using a phase contrast filter (PCF) with $60\ \mu\text{m}$ radius (Double Helix Optics,
597 custom design) positioned in the Fourier plane of L3. The spatial frequencies were recombined in the image
598 plane by L4, $f = 300$ mm, (Thorlabs, AC508-300-B). For more details, refer to³⁶. For parallel two-photon
599 excitation using a low NA Gaussian beam, the corrective phase mask provided by the manufacturer was
600 displayed on SLM1 and the PCF was displaced from the optical path as indicated in Figure 1. A blazed
601 diffraction grating (Richardson Gratings, 600 lines/mm) located at the focal plane of L4, a conjugate image
602 plane, disperses the different spectral frequency components of the ultrafast beam as required for temporal
603 focusing. The grating was oriented at the blaze angle to maximize light throughput. The dispersed beam
604 was collimated in one direction and Fourier transformed in the orthogonal direction by L5, $f = 500$ mm,
605 (Thorlabs, AC508-500-B), resulting in an asymmetric “line” illumination of SLM2 (Hamamatsu, LCOS
606 10468-07, 600×800 pixels, $20\ \mu\text{m}$ pitch), as described previously⁶¹. For this work, SLM2 was used for 2-
607 dimensional multiplexing of the beam, although 3-dimensional multiplexing would be possible. Phase
608 masks were generated using a weighted Gerchberg-Saxton algorithm as described previously^{48,73}. For all
609 data presented in Figures 1, 2 and 3, SLM2 was used to displace the sculpted light from the optical axis
610 and the zeroth-diffraction order, which was removed using a physical beam block positioned in a conjugate
611 image plane. Lenses 6 ($f = 500$ mm, (Thorlabs, AC508-500-B)) and 7 ($f = 300$ mm, (Thorlabs, AC508-300-
612 B)) were used to de-magnify the beam to the back focal plane of the objective lens (Nikon, CFI APO NIR,
613 x40, 0.8 NA, $f = 5$ mm) which projected the light (and re-combined the different spectral frequency
614 components) onto the focal plane. A half-wave plate was included downstream of SLM2 in path 1 to convert
615 s-polarised light to p-polarised.

616 In path 2, a Galilean beam expander formed of two lenses (L8, $f = -75$ mm, (Thorlabs, LC1258-B) and L9,
617 $f = 500$ mm, (Thorlabs, AC508-500-B)), expanded the beam onto SLM3, (Hamamatsu, LCOS X13138-07,
618 1272×1024 pixels, $12.5\ \mu\text{m}$ pitch). For the single cell experiments, 5 holograms designed to generate a
619 single $12\ \mu\text{m}$ holographic spot (located in the same position) were computed prior to each session. For
620 each recording, one of these phase masks was randomly selected and displayed on the SLM in order to
621 minimize any effects of the variable speckle distribution on the resulting dataset. The holograms displayed
622 on SLM3 were designed to generate multiple $12\ \mu\text{m}$ holographic spots targeted to chosen neurons
623 throughout the field of excitation following the calibration procedure outlined in the Supplementary
624 Information. All holograms were calculated using an iterative Gerchberg-Saxton algorithm⁷⁴. The zeroth
625 diffraction order was removed using a physical beam block positioned in a conjugate image plane. The
626 modulated beam was Fourier transformed by L10 ($f = 750$ mm, (Thorlabs, AC508-750-B)), to form the
627 holographic disks in a conjugate image plane where a blazed grating (Thorlabs, GR50-0610, 600 lines/mm)
628 was located. A 2” diffraction grating was used to maximise the field of excitation. The diffraction grating was
629 oriented perpendicular to the optical axis and the illumination angle was chosen such that the first diffraction

630 order of the central wavelength propagated along the optical axis. This orientation did not coincide with the
631 blaze angle, and hence was not the most efficient²³ but was allowed the temporal focusing plane of each
632 of the holographic disks to coincide with the focal plane of the objective lens. A pair of telescopes comprised
633 of L11 (f = 500 mm, (Thorlabs, AC508-500-B)), L12 (f = 300 mm, (Thorlabs, AC508-300-B)), L7 (f = 300
634 mm, (Thorlabs, AC508-300-B)) and the objective lens (Nikon, CFI APO NIR, x40, 0.8 NA, f = 5 mm, water)
635 was used to de-magnify and relay the holographic spots on to the sample plane. In experiments where non-
636 temporally focused spots were used (1030 nm excitation), the diffraction grating was replaced by a mirror.

637 Excitation paths 1 and 2 were combined prior to the tube lens (L7) using a polarising beam splitter (Thorlabs,
638 PBS253). The linear polarisation of the light exiting the objective was changed using a half-wave plate
639 following the PBS. For each modality, the rotation of the half-wave plate was set to that which was found
640 to maximise the two-photon excited JEDI-2P-kv fluorescence.

641 SLM1 was also used to optimise the alignment of the GPC path by translating the position of the π phase
642 disk relative to the centre of the incident Gaussian beam and adding tip/tilt/defocus phases to translate the
643 position of the focus with respect to the PCF filter. SLMs 1, 2 and 3 were also used to correct for system
644 aberrations by adjusting the coefficients of Zernike modes (evaluated at the centre of each SLM pixel) in
645 order to maximise the efficiency, uniformity and contrast of two-photon excited fluorescence excited in a
646 thin rhodamine layer.

647 In all experiments, fluorescence was captured using a simple widefield detection axis comprised of a
648 microscope objective (Nikon, CFI APO NIR, x40, 0.8 NA, f = 5 mm, water), a tube lens (TL), (Thorlabs,
649 TTL200-A) and a scientific complementary metal-oxide semiconductor (sCMOS) camera (Hamamatsu
650 ORCAFlash 4.0 or Photometrics Kinetix, as summarised in Supplementary Table 1). For both sCMOS
651 detectors, the pixel size at the sample plane was 0.1625 μm and 1x1 binning was used for all experiments.
652 The fluorescence was separated from the excitation light using a dichroic mirror (Semrock #FF705-Di01,
653 70 x 50 mm). Widefield, single photon, epi-fluorescence excitation was accomplished by means of two LED
654 sources (Thorlabs M490L4, 490 nm to excite JEDI-2P-kv fluorescence and Thorlabs M430L5, 430 nm to
655 excite BFP fluorescence), filtered by bandpass excitation filters (Semrock FF02-482/18, FF01-414/46) and
656 focused onto the back focal plane of the objective lens by means of an achromatic lens (Thorlabs f = 50
657 mm). Long exposure times (1s) and low excitation power densities were used to acquire all images based
658 on single photon fluorescence. For single photon or dual-colour imaging (for instance during all-optical
659 experiments), fluorescence was filtered using either a quad-band filter (Chroma ZET405/488/561/640) or
660 individual bandpass filters (Chroma ET525/50, ET605/7). Infrared light used for two-photon excitation of
661 fluorescence was blocked from the camera using a shortpass filter (Semrock #FF01-750sp).

662 Data were acquired using a control scheme based on custom scripts written to control *micro-manager 2.0*
663 *Gamma*⁷⁵ from Python via Pycro-manager⁷⁶. All experiments were controlled using two desktop computers
664 running Windows 10. During voltage imaging experiments, the micro-manager acquisition engine was
665 bypassed. Data from the camera was streamed directly to disk on one of the acquisition computers. The

666 first step of any experiment was to acquire 2 (JEDI-2P-kv and transmitted light) or 3 (JEDI-2P-kv, ChroME-
667 ST (H2B-BFP2) and transmitted light) widefield images of the sample. These images were used to select
668 targeted cells during a given experiment. The centroids of all targeted cells were written to file for all
669 experiments. All widefield images presented in this text are background subtracted for visualization
670 purposes (rolling ball background subtraction, ImageJ, rolling ball radius 50 pixels). All the voltage imaging
671 data presented in this manuscript were acquired in “dynamic range”, 16-bit mode, which meant that a
672 maximum of 266 rows of pixels could be acquired at 1 kHz ($43 \times 250 \mu\text{m}^2$ FOV). In practice we used an
673 exposure time of 1 ms resulting in an effective acquisition rate of 980 Hz following 0.02 ms readout (similarly
674 for the recordings referred to as 500 and 750 Hz in the manuscript). For single cell experiments
675 (corresponding to data presented in Figures 2-5), data were only acquired for a square region with diameter
676 less than 266 pixels centred on a given cell. For the multi-cell experiments, neurons were grouped to find
677 the maximal number which could be imaged within 266 pixels. The relative centroids of all targeted cells
678 within this cropped region, and the upper left-hand coordinate of each cropped region were written to file
679 for all experiments. These coordinates were used to “stitch” data from sequential acquisitions into a single
680 dataset. In “dynamic range” mode, the field of view is inversely proportional to the exposure time, such that
681 we could acquire data from 532 rows ($86 \times 250 \mu\text{m}^2$ FOV) at 500 Hz. The field of view could be increased
682 by a factor of 6 using “speed” mode, where data is read out at 8-bit. The camera was triggered using a 5
683 V, TTL signal generated by pCLAMP (Molecular Devices, Sunnyvale, CA) controlling an acquisition system
684 (Molecular Devices, Axon Digidata 1550B). During experiments, widefield images were visualised using
685 the open-source image viewer Napari and voltage imaging traces were visualised using pyqtgraph.

686 All fluorescence traces were analysed using the same analysis pipeline written in Python, as outlined in the
687 main text and Supplementary Information, derived from⁵⁰. When multiple cells were imaged simultaneously,
688 the (known) centroid of the excitation spot in camera co-ordinates was used to crop a rectangular region of
689 interest (ROI) surrounding each cell (generally 100×100 pixels). In rare cases where the ROIs of
690 independent cells overlapped, a region of each independent cell was identified manually. Individual cells
691 were then defined according by regression of each pixel in the ROI against the average fluorescence trace
692 of the manually segmented pixels.

693 **Preparation of CHO cells**

694 CHO cells were acquired from Sigma (Sigma, 85050302) and cultured in T25 flasks (Falcon, 353107) in a
695 medium consisting of DMEM-F12 + Glutamax (Fisher, Gibco™ 10565018), supplemented with 10% SBF
696 (Fisher, Gibco™ 10500-064) and 1% penicillin/streptomycin (5000 U ml^{-1}). Cells were passaged every 2-3
697 days. Prior to each experiment, cells were seeded on coverslips (Fisher, 10252961) in 24-well plates (50
698 000 cells/ml). After 24 hours, cells were transiently transfected with a plasmid using the Jet prime kit
699 (Ozyme, POL101000015) (Table 1). The medium was then replaced after 4 hours. Experiments were
700 performed 48 hours post transfection.

701 Table 1: List of plasmids

Plasmid	Transfection ratio
pAAV_hSyn_JEDI-2P_GSS3_Kv2.1	0.75 µg DNA: 1.5 µl transfectant
pAAV_CamKIIa_ChRoME-ST_P2A_H2B_BFP	0.75 µg DNA: 1.5 µl transfectant

702 **Electrophysiology for scanless two-photon voltage imaging in CHO cells**

703 48 hours post transfection, whole-cell voltage clamp recordings of JEDI-2P-kv-expressing CHO cells were
 704 performed at room temperature (21 - 23°C). An upright microscope (Scientifica, SliceScope) was equipped
 705 with a far-red LED (Thorlabs, M660L4), oblique condenser, microscope objective (Nikon, CFI APO NIR,
 706 40X, 0.8 NA), tube lens (Thorlabs, TTL200-A), and an sCMOS camera (Photometrics, Kinetix, or
 707 Hamamatsu, Flash4.0) to collect light transmitted through the sample. Patch clamp recordings were
 708 performed using an amplifier (Molecular Devices, Multiclamp 700B), a digitizer (Molecular Devices, Digidata
 709 1550B) at a sampling rate of 10 kHz and controlled using pCLAMP11 (Molecular Devices). Cells were
 710 continuously perfused with artificial cerebrospinal fluid (ACSF) comprised of 125 mM NaCl, 2.5 mM KCl,
 711 1.5 mM CaCl₂, 1 mM MgCl₂, 26 mM NaHCO₃, 0.3 mM ascorbic acid, 25 mM D-glucose, 1.25 mM NaH₂PO₄.
 712 Continuous aeration of the recording solution with 95% O₂ and 5% CO₂, resulted in a final pH of 7.4
 713 (measured). Borosilicate pipettes (with filament, OD: 1.5 mm, ID: 0.86 mm, 10 cm length, fire polished,
 714 WPI) were pulled using a Sutter Instruments P1000 puller, to a tip resistance of 3.5–6 MΩ. Pipettes were
 715 filled with an intracellular solution consisting of 135 mM K-gluconate, 4 mM KCl, 4 mM Mg-ATP, 0.3 mM
 716 Na₂-GTP, 10 mM Na₂-phosphocreatine, and 10 mM HEPES (pH 7.35). All membrane potentials reported in
 717 this manuscript are Liquid Junction Potential (LJP) corrected by -15 mV (measured). Recordings were
 718 compensated for capacitance (Cm) and series resistance (Rs) to 70 % (Cm = 11.6 ± 4.7 pF; Rs = 16.1 ±
 719 8.2 MΩ; mean ± s.d.). Only recordings with an access resistance below 35 MΩ were included in subsequent
 720 analysis.

721
 722 All experiments were performed with laser A, except data presented in Supplementary Figure 20 where
 723 laser C was used.

724
 725 For protocols 1 and 2 (Figure 2), JEDI-2P-kv-expressing CHO cells were patched and clamped at -55 mV
 726 and 3, 100 mV steps were applied under either continuous (3 s, power density: 0.88 mW µm⁻²,
 727 corresponding to 100 mW per cell) or strobed illumination (200 ms every 2.5 s, power densities ranging
 728 from 0.66 to 1.55 mW µm⁻² (75 to 175 mW per cell), as specified in the main text). The fluorescent responses
 729 to the depolarization steps were simultaneously recorded at 100 Hz. For protocol 3, JEDI-2P-kv-expressing
 730 CHO cells were patched and clamped at -75 mV to mimic the resting potential of neurons in the dentate
 731 gyrus of hippocampal organotypic slices. A 20 Hz train of 10, 3 ms, 100 mV steps was electrically induced,

732 and the fluorescent response to different scanless illumination methods was recorded simultaneously (500
733 ms, power density: $1.33 \text{ mW } \mu\text{m}^{-2}$, corresponding to 150 mW per cell, 1 kHz acquisition).

734

735 The ability to record voltage responses using JEDI-2P-kv under 1030 nm illumination was assessed using
736 protocol 2 with a holographic spot (12 μm diameter, not temporally focused, power density: $0.4 \text{ mW } \mu\text{m}^{-2}$,
737 corresponding to 45 mW per cell, Supplementary Figure 19).

738

739 For data presented in Supplementary Figure 20, ChromE-ST expressing cells were patched in whole cell
740 voltage clamp configuration at -55 mV and photocurrents in response to 17.5 ms pulses of light (power
741 densities ranging from 0.02 to $0.04 \text{ mW } \mu\text{m}^{-2}$, corresponding to 2.5 to 5 mW per cell) were recorded.

742

743 **Preparation of hippocampal organotypic slice cultures for validating scanless two-photon voltage** 744 **imaging of neuronal activity using JEDI-2P-kv**

745 All experimental procedures were conducted in accordance with guidelines from the European Union and
746 institutional guidelines on the care and use of laboratory animals (Council Directive 2010/63/EU of the
747 European Union). Hippocampal organotypic slices were prepared from mice (Janvier Labs, C57Bl6J) at
748 postnatal day 8 (P8). Hippocampi were sliced with a tissue Chopper (McIlwain type 10180, Ted Pella) into
749 $300 \mu\text{m}$ thick sections in a cold dissecting medium consisting of GBSS (Sigma, G9779) supplemented with
750 25 mM D-glucose, 10 mM HEPES, 1 mM Na-Pyruvate, 0.5 mM α -tocopherol, 20 nM ascorbic acid, and 0.4%
751 penicillin/streptomycin (5000 U ml^{-1}).

752 After 30 - 45 min of incubation at $4 \text{ }^\circ\text{C}$ in the dissecting medium, slices were placed onto a porous membrane
753 (Millipore, Millicell CM PICM03050) and cultured at $37 \text{ }^\circ\text{C}$, 5% CO_2 in a medium consisting of 50% Opti-
754 MEM (Fisher 15392402), 25% heat-inactivated horse serum (Fisher 10368902), 24% HBSS, and 1%
755 penicillin/streptomycin (5000 U ml^{-1}). This medium was supplemented with 25 mM D-glucose, 1 mM Na-
756 Pyruvate, 20 nM ascorbic acid, and 0.5 mM α -tocopherol. After three days in-vitro (DIV), the medium was
757 replaced with one containing 82% neurobasal-A (Fisher 11570426), 15% heat-inactivated horse serum
758 (Fisher 11570426), 2% B27 supplement (Fisher, 11530536), 1% penicillin/streptomycin (5000 U ml^{-1}),
759 which was supplemented with 0.8 mM L-glutamine, 0.8 mM Na-Pyruvate, 10 nM ascorbic acid and 0.5 mM
760 α -tocopherol. This medium was removed and replaced once every 2-3 days.

761 Slices were transduced with AAV9_hSyn_JEDI-2P_Kv2.1 at DIV 3 by bulk application of $1 \mu\text{l}$ of virus per
762 slice (see Table 2). Experiments were performed between DIV 7 and 15.

763

764

765

766 **Electrophysiology for validating scanless two-photon voltage imaging of neuronal activity using**
767 **JEDI-2P-kv in hippocampal organotypic slices**

768 At DIV 10-15, whole-cell patch clamp recordings of JEDI-2P-kv expressing granule cells in DG were
769 performed at temperatures varying between 31-35°C. During experiments, slices were perfused with ACSF
770 as previously described. This extracellular solution was supplemented with 1 μ M AP5 (Abcam, ab120003)
771 and 1 μ M NBQX (Abcam, ab120046) in all experiments except for the spontaneous activity recordings
772 (Figures 5-6, Supplementary Figures 14 and 18). Patch pipettes were filled with intracellular solution (see
773 above).

774 Neurons were held at -75 mV in voltage clamp configuration and recordings were compensated for
775 capacitance (C_m) and series resistance (R_s) to 70 % ($C_m = 21 \pm 6.3$ pF; $R_s = 19.2 \pm 8.5$ M Ω ; mean \pm s.d.).
776 In current clamp configuration, neurons were injected with some current (less than 100 pA) if necessary to
777 maintain their resting membrane potential to -75 mV. In the latter configuration, bridge potential was
778 corrected (Bridge potential = 13.9 ± 4.2 M Ω ; mean \pm s.d.).

779 Neurons were first patched in whole-cell voltage clamp configuration. Protocol 1 was then performed to
780 confirm that the fluorescence of the patched cell was voltage responsive (Supplementary Figure 12).

781 The ability to record single action potentials in neurons (Figure 3c and d) was assessed by electrically
782 triggering a 1 Hz train of 50 action potentials with short latency and jitter under strobed illumination (10 ms,
783 power densities ranging from 0.66 to 1.55 mW μ m⁻², corresponding to 75 to 175 mW per cell) while
784 recording at three different acquisition rates (500 Hz, 750 Hz and 1 kHz). Action potentials were triggered
785 by injecting 700-900 pA currents for 2 ms.

786 Then, to assess the ability to record fast spike trains in neurons, trains of 10 action potentials from 25 to
787 125 Hz were electrically induced under illumination at different power densities (from 0.66 to 1.55 mW μ m⁻²
788 ², corresponding to 75 to 175 mW per cell) and recorded at acquisition rates varying between 500 Hz, 750
789 Hz and 1 kHz. The amount of current injected was one that was sufficient to evoke 10 action potentials at
790 each of the different spike trains. Recordings where one action potential was missing in the
791 electrophysiological trace were dismissed. 125 Hz was found to be the limit at which the granule cells could
792 spike in our conditions (Figure 3e-f and Supplementary Figure 13).

793 For data presented in Figure 4, 6, 20 ms steps separated by 30 ms and ranging from 0 to 2.5 mV (in 0.5
794 mV steps) were induced in JEDI-2P-kv expressing neurons under strobed illumination (40 ms centered
795 around the steps, power density: 1.33 mW μ m⁻², corresponding to 150 mW per cell) while recording the
796 fluorescence response at 1 kHz. This was repeated 50 - 75 times.

797 To record spontaneous activity (Figure 5), JEDI-2P-kv expressing neurons were patched and their
798 membrane potential was monitored under continuous illumination for 30 s at a power density of 1.33 mW

799 μm^2 (150 mW per cell) while recording the fluorescent response at 1 kHz. Cells were not patched for the
800 recordings presented in Supplementary Figure 14. The same protocol was repeated to perform long-term
801 voltage imaging of JEDI-2P-kv expressing neurons for a maximum of 20 min with a dark period of <10 s in
802 between each recording (due to limitations in data transfer rates). To overcome this issue, we performed
803 longer recordings (1 min) at a lower acquisition rate (500 Hz) with the same power density (1.33 mW μm^2 ,
804 corresponding to 150 mW per cell). This allowed us to shorten the dark period in between recordings to
805 < 5 s (Supplementary Figure 15).

806 The axial resolution of JEDI-2P-kv (Supplementary Figure 12) was measured by electrically triggering an
807 action potential and measuring the fluorescence response while displacing the objective in the z axis (from
808 +50 to -50 μm , in 5 μm steps). The lateral resolution was measured (from +20 to -20 μm , in 2 μm steps) by
809 mechanically moving the sample in the x-y axis.

810 To measure the performances of JEDI-2P-kv under 1030 nm illumination, hippocampal organotypic slices
811 were infected with a mixture of AAV1_EF1a_DIO_JEDI-2P_Kv2.1_WPRE and
812 AAV9_hSyn_Cre_WPRE_hGH (see Table 2) at DIV 3 in order to get a sparser expression. Isolated
813 expressing cells in the dentate gyrus were then patched in whole cell current clamp configuration and
814 illuminated with a holographic spot (12 μm diameter, not temporally focused) at 1030 nm (power density:
815 1.21 mW μm^2 , corresponding to 137 mW per cell). Single action potentials and spontaneous activity
816 recordings were obtained as described previously (Supplementary figure 19).

817 **Preparation of hippocampal organotypic slices for two-photon actuation and imaging of neural** 818 **activity using ChromE-ST and JEDI-2P-kv**

819 All animal procedures followed national and European animal care guidelines (Directive 2010/63/EU) and
820 institutional guidelines on animals used for research purposes. Hippocampal organotypic slice preparations
821 were prepared as described in reference⁷⁷ with a few modifications. Briefly, hippocampi were extracted
822 from P5-P8 C56Bl/6J mouse pups sacrificed by decapitation. The dissection was carried out in filter
823 sterilized (0.2 μm pore size) ice cold medium containing: 248 mM sucrose, 26 mM NaHCO_3 , 10 mM glucose,
824 4 mM KCl, 5 mM MgCl_2 , 1 mM CaCl_2 , 2 mM kynurenic acid and 0.001 % phenol red saturated with 95 %
825 O_2 / 5 % CO_2 . Transverse slices of 300 – 400 μm thickness were cut with Mcllwain Tissue Chopper using
826 double edge stainless steel razor blades. Using a plastic transfer pipette, undamaged slices were
827 individually transferred onto the small pieces of PTFE membrane (Millipore FHLP04700) placed on
828 membrane inserts (Millicell PICMORG50) in the 6-well-plate containing 1 mL pre-warmed culture medium.
829 The slices were cultured at 37 °C and 5 % CO_2 in antibiotic free culture medium consisting of 80 % MEM
830 and 20 % Heat-inactivated horse serum supplemented with 1 mM L-glutamine, 0.01 mg/ml Insulin, 14.5
831 mM NaCl, 2 mM MgSO_4 , 1.44 mM CaCl_2 , 0.00125 % Ascorbic acid and 13mM D-glucose. The culture
832 medium was partially replaced with fresh, 37 °C warmed culture medium every 3 days.

833 Various titrations were tested to achieve sufficient levels of expression of both sensor and actuator. When
 834 slices were transduced with both viruses on the same day, we observed a reduction in the expression of
 835 JEDI-2P-kv. Furthermore, overexpression-mediated apoptosis was observed in some cases when slices
 836 were transduced with both viruses simultaneously. The best results were obtained by transducing slices
 837 with JEDI-2P-kv first, followed a week later by ChroME-ST which resulted in strong co-expression of both
 838 proteins (Figure 8a). However, in general we found that the expression levels of both proteins were more
 839 variable when the two constructs were co-expressed than when either construct was expressed
 840 independently.

841 Slices were transduced firstly with AAV9-hSyn-JEDI-2P-Kv2.1 at DIV 3 and secondly with
 842 AAV9_Camk2a_ChroME-ST_P2A_H2B_tagBFP2 (provided by H. Adesnik, University of California,
 843 Berkeley, USA) at DIV 10 by bulk application of 1 μ l of virus per slice (Table 2). Channelrhodopsin-
 844 expressing cells were visualized using stable expression of an H2B-BFP2 fusion, which resulted in nuclear
 845 localized BFP2 fluorescence. Experiments were performed between DIV 13 and 17.

846 To characterize the performances of ChroME-ST (Figure 7), ChroME-ST and JEDI-2P-kv co-expressing
 847 granule cells in DG were patched in whole-cell current clamp configuration. 5, 17.5 ms pulses of light at 5
 848 Hz were applied at different power densities ranging from 0 to 0.09 $\text{mW } \mu\text{m}^{-2}$ (0 to 10 mW per cell) to photo-
 849 evoke action potentials. The fluorescent responses were recorded at an acquisition rate of 1 kHz. The
 850 latency and jitter of light-evoked action potentials, respectively defined as the mean and standard deviation
 851 of the time between the onset of stimulation and the peak of the action potential, were measured using the
 852 same protocol. The axial resolution of ChroME-ST was measured using a similar protocol, while displacing
 853 the spot axially by mechanically moving the objective from +75 to -50 μm , in 5 μm steps in the vicinity of
 854 the cell (from +55 μm to -10 μm) and then in 10 μm steps (Figure 7 and Supplementary Figure 20).

855 For each cell, the power density was increased until a spike was detected optically in at least one of five
 856 repeats. The final set of power densities used was between 0.02 – 0.08 $\text{mW } \mu\text{m}^{-2}$ (2.5 – 9 mW) per cell.

857 Table 2: List and final titres of viruses

Virus	Final titer (vg ml ⁻¹)
AAV9_hSyn_JEDI-2P_GSS3_Kv2.1	3.12×10^{13}
AAV9_CamKIIa_ChRoME-ST_P2A_H2B_BFP	4.46×10^{12}
AAV1_EF1a_DIO_JEDI-2P_Kv2.1_WPRE	2.36×10^{13}
AAV9_hSyn_Cre_WPRE_hGH	2.3×10^{11}

858

859

860 **Immunostaining**

861 Immunostaining was performed on hippocampal organotypic slices to assess the potential non-linear
862 photodamage induced by two different laser sources (A and C) during our experiments.

863 In the case of laser A, slices expressing JEDI-2P-kv were illuminated with a holographic spot (12 μm
864 diameter, temporally focused, power densities between 0.66 – 1.55 $\text{mW } \mu\text{m}^{-2}$, corresponding to 75 – 175
865 mW per cell) in the dentate gyrus. The illumination protocol consisted of 50, 10 ms pulses of light, using the
866 same protocol used to record single action potentials (see previous section), repeated on > 15 cells per
867 region illuminated. A negative control (no illumination) and a positive control where a whole region was
868 continuously illuminated for 30 min (power density: 1.64 $\text{mW } \mu\text{m}^{-2}$, corresponding to 185 mW per cell) were
869 also performed.

870 Slices expressing JEDI-2P-kv and ChromE-ST were illuminated with 5 holographic spots generated with
871 laser source C (12 μm diameter, power densities ranging between 0.02 – 0.09 $\text{mW } \mu\text{m}^{-2}$ (2.5 – 10 mW per
872 cell), 45 μm separation), and moved laterally across 120 μm in 20 μm steps. The illumination protocol used
873 to characterize the ChromE-ST (see previous section) was repeated 5 times at each position, and the
874 hologram was recomputed each time.

875 After experiments, slices were immediately fixed in PFA 4% for 3-5 min. Permeabilization of the tissue was
876 performed by incubation of the slice in a solution comprising of Triton X-100 in PBS (0.5 %) for 12 hours at
877 4 °C. Non-specific sites were then blocked by incubation in a blocking solution (BSA 20 % in PBS) for 4
878 hours at room temperature (21-23 °C).

879 Slices were incubated with primary antibodies diluted in a solution of BSA 5 % in PBS (Table 3) overnight
880 at 4 °C and placed in a solution of BSA 5 % in PBS on a horizontal shaker for 10 minutes to wash off excess
881 antibodies. This process was repeated three times.

882 Slices were then incubated with species-appropriate secondary antibodies conjugated to Alexa fluor 555 (to
883 detect anti-activated-Caspase-3 immunostaining) and Alexa fluor 647 (to detect anti-HSP70/72
884 immunostaining) diluted in the same solution as the primary ones, for 3-4 hours at room temperature (21-
885 23 °C). They were then washed again following the same process, but in PBS only.

886 Slices were immediately mounted in Fluoromount-g mounting medium (Southern Biotech, 0100-01) to be
887 imaged using confocal microscopy (Olympus FV3000, 20X magnification, 0.8 NA, pixel size 0.6214 μm , λ
888 488, 561, 640 nm). The same imaging parameters were used for all experimental conditions.

889

890 Table 3: List and dilutions of antibodies used for immunostaining

Antibody	Supplier	Reference	Species	Working dilution
HSP70 / HSP72	Enzo Life Science	ADI-SPA-810-D	Mouse	1:400
Cleaved Caspase-3 (Asp175)	Cell Signaling	9661	Rabbit	1:250
Anti-mouse, Alexa fluor 647	Thermofisher Scientific	A21235	Goat	1:500
Anti-rabbit, Alexa fluor 555	Thermofisher Scientific	A21429	Goat	1:500

891

892 **Statistics**

893 All experiments were repeated for at least two (and generally many more) independent passages of cells,
 894 transfections or infections. The Shapiro test (`scipy.stats.shapiro`) was used to test whether data were
 895 normally distributed. For normally distributed data, the paired or unpaired two-tailed students t-test was
 896 used to compare two independent samples. The non-parametric Mann-Whitney *U*-test
 897 (`scipy.stats.mannwhitneyu`) was used to compare two samples in the case when either or both samples
 898 were found not to be normally distributed. 'n' refers to the number of independent biological replicates, as
 899 stated in each figure caption and summarized in Supplementary Table 2. A statistical comparison was
 900 deemed significant if the p-value was less than 0.05. For all figures * denotes $p < 0.05$, ** denotes $p < 0.01$
 901 and *** denotes $p < 0.0001$. All results reported in the manuscript are communicated as the mean value \pm
 902 standard deviation of at least three technical replicates unless otherwise stated. As specified, error bars in
 903 plots denote either the standard deviation or the standard error. All biological replicates were included in
 904 each estimate. Estimation stats were performed using the Python package `dabestr`⁷⁸.

905

906 **References**

- 907 1. Scanziani, M. & Hausser, M. Electrophysiology in the age of light. *Nature* **461**, 930–939 (2009).
- 908 2. Emiliani, V. *et al.* Optogenetics for light control of biological systems. *Nat. Rev. Methods Prim.* **2**,
909 55 (2022).
- 910 3. Abdelfattah, A. *et al.* Neurophotonic Tools for Microscopic Measurements and Manipulation:
911 Status Report. *Neurophotonics* **9**, 1–86 (2022).
- 912 4. Clapham, D. E. Calcium Signaling. *Cell* **131**, 1047–1058 (2007).
- 913 5. Grienberger, C. & Konnerth, A. Imaging Calcium in Neurons. *Neuron* **73**, 862–885 (2012).
- 914 6. Tsien, R. Y. New calcium indicators and buffers with high selectivity against magnesium and
915 protons: design, synthesis, and properties of prototype structures. *Biochemistry* **19**, 2396–2404
916 (1980).
- 917 7. Tian, L., Andrew Hires, S. & Looger, L. L. Imaging neuronal activity with genetically encoded
918 calcium indicators. *Cold Spring Harb. Protoc.* **7**, 647–656 (2012).
- 919 8. Chen, Y. *et al.* Soma-Targeted Imaging of Neural Circuits by Ribosome Tethering. *Neuron* **107**,
920 454-469.e6 (2020).
- 921 9. Shemesh, O. A. *et al.* Precision Calcium Imaging of Dense Neural Populations via a Cell-Body-
922 Targeted Calcium Indicator. *Neuron* **107**, 470-486.e11 (2020).
- 923 10. Zhu, M. H., Jang, J., Milosevic, M. M. & Antic, S. D. Population imaging discrepancies between a
924 genetically-encoded calcium indicator (GECI) versus a genetically-encoded voltage indicator
925 (GEVI). *Sci. Rep.* **11**, 1–15 (2021).
- 926 11. Peterka, D. S., Takahashi, H. & Yuste, R. Imaging Voltage in Neurons. *Neuron* **69**, 9–21 (2011).
- 927 12. Davila, H. V, Salzberg, B. M., Cohen, L. B. & Waggoner, A. S. A Large Change in Axon
928 Fluorescence that Provides a Promising Method for Measuring Membrane Potential. *Nat. New*
929 *Biol.* **241**, 160–161 (1973).
- 930 13. Loew, L. M. *et al.* A naphthyl analog of the aminostyryl pyridinium class of potentiometric
931 membrane dyes shows consistent sensitivity in a variety of tissue, cell, and model membrane
932 preparations. *J. Membr. Biol.* **130**, 1–10 (1992).
- 933 14. Abdelfattah, A. S. *et al.* Bright and photostable chemigenetic indicators for extended in vivo
934 voltage imaging. *Science (80-.)*. **365**, 699–704 (2019).
- 935 15. Knöpfel, T. & Song, C. Optical voltage imaging in neurons: moving from technology development

- 936 to practical tool. *Nat. Rev. Neurosci.* **20**, 719–727 (2019).
- 937 16. Lu, X. *et al.* Detecting rapid pan-cortical voltage dynamics in vivo with a brighter and faster voltage
938 indicator Authors. *bioRxiv* (2022). doi:10.1101/2022.08.29.505018
- 939 17. Quicke, P. *et al.* Single-Neuron Level One-Photon Voltage Imaging With Sparsely Targeted
940 Genetically Encoded Voltage Indicators. *Front. Cell. Neurosci.* **13**, 1–12 (2019).
- 941 18. Hochbaum, D. R. *et al.* All-optical electrophysiology in mammalian neurons using engineered
942 microbial rhodopsins. *Nat. Methods* **11**, 825–833 (2014).
- 943 19. Parot, V. J. *et al.* Compressed Hadamard microscopy for high-speed optically sectioned neuronal
944 activity recordings. *J. Phys. D. Appl. Phys.* **52**, (2019).
- 945 20. Fan, L. Z. *et al.* All-Optical Electrophysiology Reveals the Role of Lateral Inhibition in Sensory
946 Processing in Cortical Layer 1. *Cell* **180**, 521-535.e18 (2020).
- 947 21. Xiao, S. *et al.* Large-scale voltage imaging in behaving mice using targeted illumination. *iScience*
948 **24**, (2021).
- 949 22. Fisher, J. A. N., Salzberg, B. M. & Yodh, A. G. Near infrared two-photon excitation cross-sections
950 of voltage-sensitive dyes. *J Neurosci Methods* **148**, 94–102 (2005).
- 951 23. Sims, R. R. *et al.* Optical manipulation and recording of neural activity with wavefront engineering.
952 in *Neuromethods* (ed. Papagiakoumou, E.) **191**, (Humana Press New York, 2023).
- 953 24. Acker, C. D., Yan, P. & Loew, L. M. Single-voxel recording of voltage transients in dendritic spines.
954 *Biophys. J.* **101**, L11–L13 (2011).
- 955 25. Roome, C. J. & Kuhn, B. Simultaneous dendritic voltage and calcium imaging and somatic
956 recording from Purkinje neurons in awake mice. *Nat. Commun.* **9**, 1–14 (2018).
- 957 26. Brinks, D., Klein, A. J. & Cohen, A. E. Two-Photon Lifetime Imaging of Voltage Indicating Proteins
958 as a Probe of Absolute Membrane Voltage. *Biophys. J.* **109**, 914–921 (2015).
- 959 27. Fisher, J. a N. *et al.* Two-photon excitation of potentiometric probes enables optical recording of
960 action potentials from mammalian nerve terminals in situ. *J. Neurophysiol.* **99**, 1545–1553 (2008).
- 961 28. Wu, J. *et al.* Kilohertz two-photon fluorescence microscopy imaging of neural activity in vivo. *Nat.*
962 *Methods* **17**, 287–290 (2020).
- 963 29. Villette, V. *et al.* Ultrafast Two-Photon Imaging of a High-Gain Voltage Indicator in Awake
964 Behaving Mice. *Cell* **179**, 1590-1608.e23 (2019).
- 965 30. Platasa, J. *et al.* High-Speed Low-Light In Vivo Two-Photon Voltage Imaging of Large Neuronal

- 966 Populations. *bioRxiv* 2021.12.07.471668 (2021). doi:10.1101/2021.12.07.471668
- 967 31. Kulkarni, R. U. *et al.* In Vivo Two-Photon Voltage Imaging with Sulfonated Rhodamine Dyes. *ACS*
968 *Cent. Sci.* **4**, 1371–1378 (2018).
- 969 32. Kazemipour, A. *et al.* Kilohertz frame-rate two-photon tomography. *Nat. Methods* **16**, 778–786
970 (2019).
- 971 33. Bando, Y., Wenzel, M. & Yuste, R. Simultaneous two-photon imaging of action potentials and
972 subthreshold inputs in vivo. *Nat. Commun.* **12**, 1–12 (2021).
- 973 34. Cornejo, V. H., Ofer, N. & Yuste, R. Voltage compartmentalization in dendritic spines in vivo.
974 *Science (80-.)*. **375**, 82–86 (2022).
- 975 35. Li, B. *et al.* Two-Photon Voltage Imaging of Spontaneous Activity from Multiple Neurons Reveals
976 Network Activity in Brain Tissue. *iScience* **23**, 101363 (2020).
- 977 36. Papagiakoumou, E. *et al.* Scanless two-photon excitation of channelrhodopsin-2. *Nat. Methods* **7**,
978 848–854 (2010).
- 979 37. Papagiakoumou, E., de Sars, V., Oron, D. & Emiliani, V. Patterned two-photon illumination by
980 spatiotemporal shaping of ultrashort pulses. *Opt. Express* **16**, 22039–22047 (2008).
- 981 38. Papagiakoumou, E. *et al.* Functional patterned multiphoton excitation deep inside scattering
982 tissue. *Nat. Photonics* **7**, 274–278 (2013).
- 983 39. Pégard, N. M., Oldenburg, I., Sridharan, S., Waller, L. & Adesnik, H. 3D scanless holographic
984 optogenetics with temporal focusing. *Nat. Commun.* **8**, 1228 (2017).
- 985 40. Liu, Z. *et al.* Sustained deep-tissue voltage recording using a fast indicator evolved for two-photon
986 microscopy. *Cell* **185**, 3408–3425.e29 (2022).
- 987 41. Oron, D., Tal, E. & Silberberg, Y. Scanningless depth-resolved microscopy. *Opt. Express* **13**,
988 1468–1476 (2005).
- 989 42. Zhu, G., van Howe, J., Durst, M., Zipfel, W. & Xu, C. Simultaneous spatial and temporal focusing
990 of femtosecond pulses. *Opt. Express* **13**, 2153–2159 (2005).
- 991 43. Papagiakoumou, E., Ronzitti, E. & Emiliani, V. Scanless two-photon excitation with temporal
992 focusing. *Nat. Methods* **17**, 571–581 (2020).
- 993 44. Mardinly, A. R. *et al.* Precise multimodal optical control of neural ensemble activity. *Nat. Neurosci.*
994 **21**, 881–893 (2018).
- 995 45. Bègue, A. *et al.* Two-photon excitation in scattering media by spatiotemporally shaped beams and

- 996 their application in optogenetic stimulation. *Biomed. Opt. Express* **4**, 2869–2879 (2013).
- 997 46. Dal Maschio, M., Donovan, J. C., Helmbrecht, T. O. & Baier, H. Linking Neurons to Network
998 Function and Behavior by Two-Photon Holographic Optogenetics and Volumetric Imaging. *Neuron*
999 **94**, 774-789.e5 (2017).
- 1000 47. Golan, L., Reutsky, I., Farah, N. & Shoham, S. Design and characteristics of holographic neural
1001 photo-stimulation systems. *J. Neural Eng.* **6**, 66004 (2009).
- 1002 48. Yang, S. *et al.* Three-dimensional holographic photostimulation of the dendritic arbor. *J. Neural*
1003 *Eng.* **8**, 46002 (2011).
- 1004 49. Xie, M. E. *et al.* High-fidelity estimates of spikes and subthreshold waveforms from 1-photon
1005 voltage imaging in vivo. *Cell Rep.* **35**, (2021).
- 1006 50. Cai, C. *et al.* VolPy: Automated and scalable analysis pipelines for voltage imaging datasets. *PLoS*
1007 *Comput. Biol.* **17**, 1–27 (2021).
- 1008 51. Kralj, J. M., Douglass, A. D., Hochbaum, D. R., Maclaurin, D. & Cohen, A. E. Optical recording of
1009 action potentials in mammalian neurons using a microbial rhodopsin. *Nat. Methods* **9**, 90–5
1010 (2012).
- 1011 52. Hopt, A. & Neher, E. Highly nonlinear photodamage in two-photon fluorescence microscopy.
1012 *Biophys. J.* **80**, 2029–36 (2001).
- 1013 53. Quicke, P., Howe, C. L. & Foust, A. J. Balancing the fluorescence imaging budget for all-optical
1014 neurophysiology experiments. in *Neuromethods* (ed. Papagiakoumou, E.) **191**, (Humana Press
1015 New York, 2023).
- 1016 54. Blankenship, A. G. & Feller, M. B. Mechanisms underlying spontaneous patterned activity in
1017 developing neural circuits. *Nat. Rev. Neurosci.* **11**, 18–29 (2010).
- 1018 55. Ronzitti, E. *et al.* Sub-millisecond optogenetic control of neuronal firing with two-photon
1019 holographic photoactivation of Chronos. *J. Neurosci.* **37**, 1246–17 (2017).
- 1020 56. Schrödel, T., Prevedel, R., Aumayr, K., Zimmer, M. & Vaziri, A. Brain-wide 3D imaging of neuronal
1021 activity in *Caenorhabditis elegans* with sculpted light. *Nat. Methods* **10**, 1013–1020 (2013).
- 1022 57. Prevedel, R. *et al.* Fast volumetric calcium imaging across multiple cortical layers using sculpted
1023 light. *Nat. Methods* **13**, 1021–1028 (2016).
- 1024 58. Demas, J. *et al.* High-speed, cortex-wide volumetric recording of neuroactivity at cellular resolution
1025 using light beads microscopy. *Nature Methods* **18**, (2021).
- 1026 59. Song, A. *et al.* Volumetric Two-photon Imaging of Neurons Using Stereoscopy (vTwINS). *Nat.*

- 1027 *Methods* **14**, 420–426 (2017).
- 1028 60. Hernandez, O. *et al.* Three-dimensional spatiotemporal focusing of holographic patterns. *Nat.*
1029 *Commun.* **7**, 11928 (2016).
- 1030 61. Accanto, N. *et al.* Multiplexed temporally focused light shaping for high-resolution multi-cell
1031 targeting. *Optica* **5**, 1478–1491 (2018).
- 1032 62. Botcherby, E. J. *et al.* Aberration-free three-dimensional multiphoton imaging of neuronal activity
1033 at kHz rates. *Proc. Natl. Acad. Sci.* **109**, 2919–2924 (2012).
- 1034 63. Botcherby, E. J., Juskaitis, R., Booth, M. J., Wilson, T. & Juškaitis, R. An optical technique for
1035 remote focusing in microscopy. *Opt. Commun.* **281**, 880–887 (2008).
- 1036 64. Nöbauer, T. *et al.* Video rate volumetric Ca²⁺ imaging across cortex using seeded iterative
1037 demixing (SID) microscopy. *Nat. Methods* **14**, 811–818 (2017).
- 1038 65. Bovetti, S. *et al.* Simultaneous high-speed imaging and optogenetic inhibition in the intact mouse
1039 brain. *Sci. Rep.* **7**, 40041 (2017).
- 1040 66. Zhang, T. *et al.* Kilohertz two-photon brain imaging in awake mice. *Nat. Methods* **16**, 1119–1122
1041 (2019).
- 1042 67. Moretti, C., Antonini, A., Bovetti, S., Liberale, C. & Fellin, T. Scanless functional imaging of
1043 hippocampal networks using patterned two-photon illumination through GRIN lenses. *Biomed.*
1044 *Opt. Express* **7**, 3958 (2016).
- 1045 68. Accanto, N. *et al.* A flexible two-photon fiberscope for fast activity imaging and precise optogenetic
1046 photostimulation of neurons in freely moving mice. *Neuron* **111**, 1–14 (2023).
- 1047 69. Moretti, C. & Gigan, S. Readout of fluorescence functional signals through highly scattering tissue.
1048 *Nat. Photonics* **14**, 361–364 (2020).
- 1049 70. Printz, Y. *et al.* Determinants of functional synaptic connectivity among amygdala-projecting
1050 prefrontal cortical neurons. (2021).
- 1051 71. Hage, T. A. *et al.* Synaptic connectivity to L2/3 of primary visual cortex measured by two-photon
1052 optogenetic stimulation. *eLife* **11**, (2022).
- 1053 72. Sridharan, S. *et al.* High-performance microbial opsins for spatially and temporally precise
1054 perturbations of large neuronal networks. *Neuron* 1–17 (2022). doi:10.1016/j.neuron.2022.01.008
- 1055 73. Di Leonardo, R., Ianni, F. & Ruocco, G. Computer generation of optimal holograms for optical trap
1056 arrays. *Opt. Express* **15**, 1913–22 (2007).

- 1057 74. Gerchberg, R. W. & Saxton, W. O. A practical algorithm for the determination of the phase from
1058 image and diffraction pictures. *Optik (Stuttg)*. **35**, 237–246 (1972).
- 1059 75. Edelstein, A. D. *et al.* Advanced methods of microscope control using μ Manager software. *J. Biol.*
1060 *Methods* **1**, e10 (2014).
- 1061 76. Pinkard, H. *et al.* Pycro-Manager: open-source software for customized and reproducible
1062 microscope control. *Nat. Methods* **18**, 226–228 (2021).
- 1063 77. Gee, C. E., Ohmert, I., Wiegert, J. S. & Oertner, T. G. Preparation of slice cultures from rodent
1064 hippocampus. *Cold Spring Harb. Protoc.* **2017**, 126–130 (2017).
- 1065 78. Ho, J., Tumkaya, T., Aryal, S., Choi, H. & Claridge-Chang, A. Moving beyond P values: data
1066 analysis with estimation graphics. *Nat. Methods* **16**, 565–566 (2019).
- 1067
- 1068

1069 **Acknowledgements**

1070 The project was supported by the 'Agence Nationale de la Recherche' through the projects SLALLOM
1071 (ANR-17-CE16-0021), HOLOPTOGEN (ANR-19-CE16-0026), LabEx LIFESENSES (ANR-10-LABX-65)
1072 and IHU FOReSIGHT (ANR-18-IAHU-01) (V.E., E.P., R.S.), the AXA research foundation (V.E.) and the
1073 European Research Council ("HOLOVIS-AdG" ERC2019-ADG-885090 to V.E.), Deutsche
1074 Forschungsgemeinschaft (DFG, German Research Foundation, Postdoc fellowship 442616457 to C.G.),
1075 the Klingenstein-Simons Fellowship Award in Neuroscience (F.S.-P.); the McNair Medical Foundation
1076 (F.S.-P.); the John S. Dunn Foundation (F.S.-P.); Welch Foundation grants Q-2016-20190330 and Q-2016-
1077 20220331 (F.S.-P.); NIH grants R01EB027145 (F.S.-P.), U01NS113294 (F.S.-P.), U01NS118288 (F.S.-P.),
1078 and R01EB032854 (F.S.-P.); and NSF grants 1707359 (F.S.-P) and 1935265 (F.S.-P.).

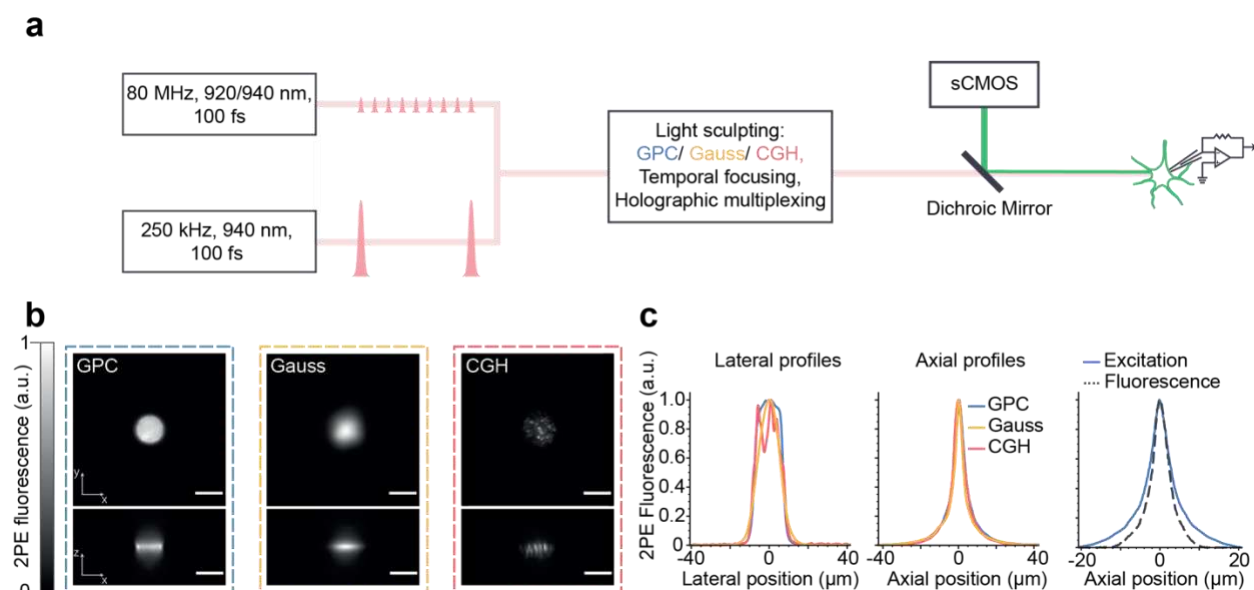
1079 We thank Yoann Zaouter and Alexandre Thai from Amplitude Systemes for the generous loan and
1080 installation of the Satsuma Niji laser, Christophe Tourain for the fabrication of custom electronic and
1081 mechanical components, Vincent de Sars for continued software development and Hillel Adesnik for the
1082 gift of the ChRoME-ST virus.

1083 We thank the viral vector facility at the Institut de la Vision for producing AAVs, the Vision Institute animal
1084 house facility for the handling of laboratory animals and Stéphane Fouquet from the Vision Institute imaging
1085 facility for technical assistance with confocal microscopy.

1086 We thank Dr. B. Arenkiel, J. Ortiz-Guzman, and Z. Chen at the TCH Neuroconnectivity Core for AAV
1087 packaging; this Core is supported by NIH grant P50HD103555 and the Charif Souki Fund.

1088

1089 **Figure 1**

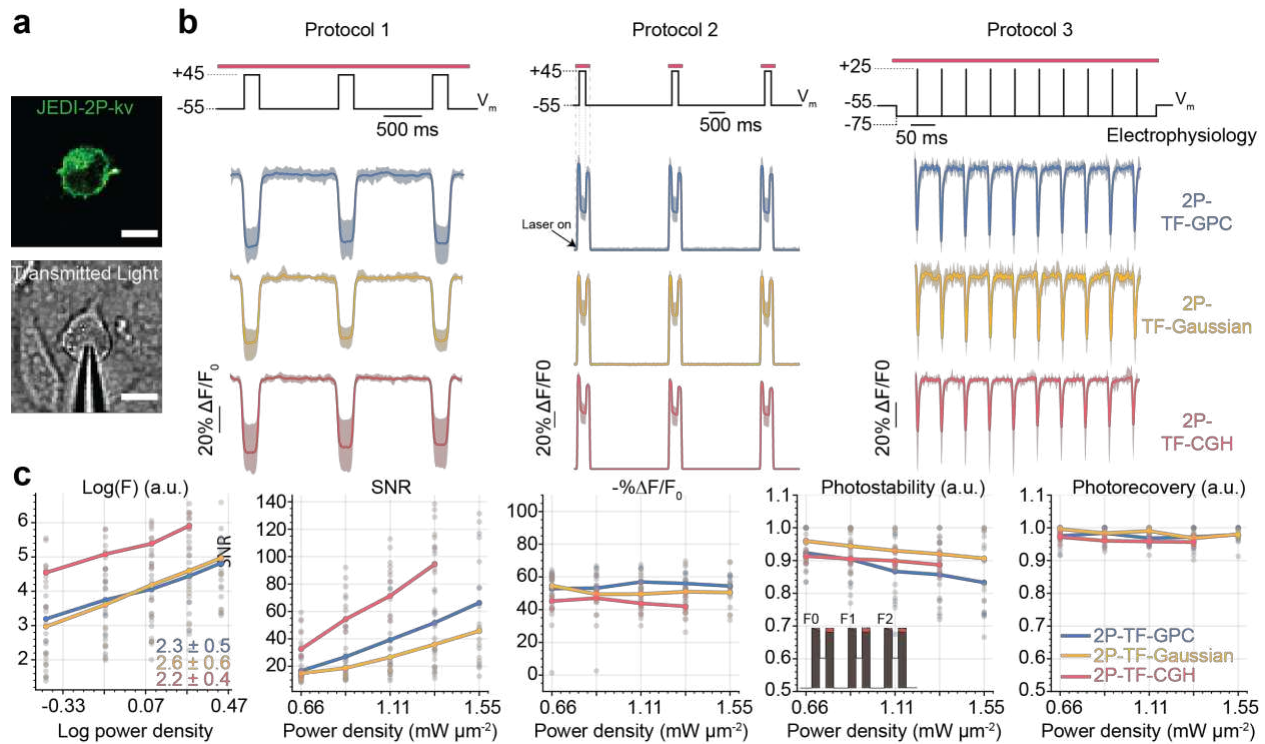


1090

1091 **Schematic and characterization of the optical setup developed for scanless two-photon voltage**
 1092 **imaging**

1093 **(a)** Summary of the optical setup designed to generate 12 μm (Full Width Half Maximum), temporally
 1094 focused, Gaussian, Generalised Phase Contrast (GPC) and holographic (CGH) spots. The setup was
 1095 equipped with three lasers, two of them delivering nJ-pulse energies at 80 MHz (Coherent Discovery, 1 W,
 1096 80 MHz, 100 fs tuned to 920, 940 or 1030 nm; Spark Alcor, 4 W, 80 MHz, 100 fs, 920 nm) and the third a
 1097 custom Optical Parametric Amplifier (OPA) pumped by an amplified fibre laser, with fixed wavelength output
 1098 (Amplitude Satsuma Niji, 0.5-0.6 W, 250 kHz, 100 fs, 940 nm). Fluorescence signals were acquired using
 1099 an sCMOS camera. The microscope was equipped for electrophysiology patch-clamp recordings. **(b)**
 1100 Lateral and axial cross sections of two-photon excited fluorescence generated with Gaussian (yellow), GPC
 1101 (blue) and GCH (red) beams, as indicated in the legend. Scale bars represent 10 μm . **(c)** Lateral and axial
 1102 profiles of two-photon excited fluorescence generated with each excitation modality, and the corresponding
 1103 system response, demonstrating single-cell resolution.

1104

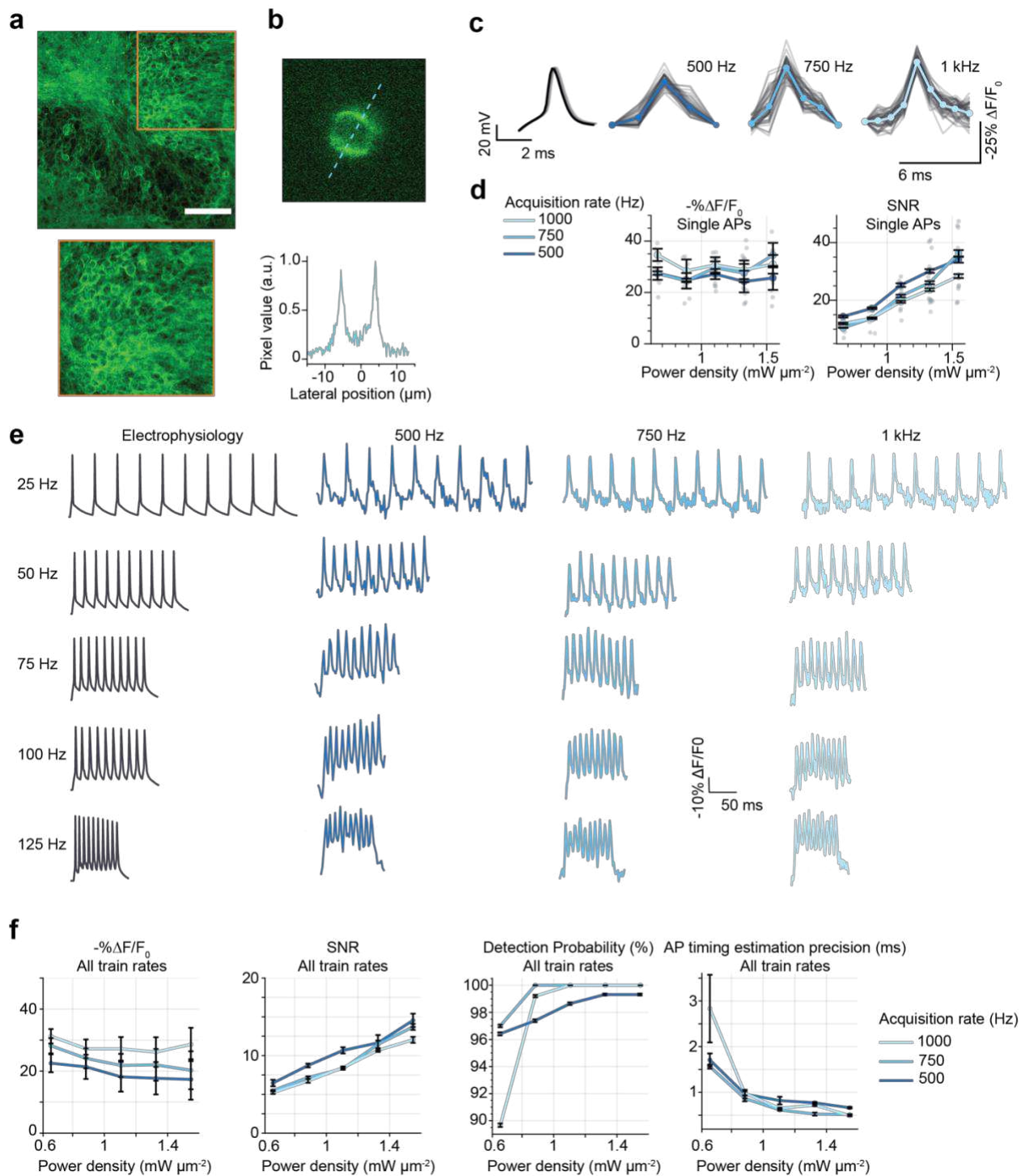


1106

1107 **In-vitro electrophysiological characterisation of scanless two-photon voltage imaging in cultured** 1108 **CHO cells.**

1109 **(a)** Confocal image of a JEDI-2P-kv expressing CHO cell (upper) and transmitted light image of a patched
1110 CHO cell (lower). Scale bars represent 10 μm . **(b)** Data from three protocols used to test the performance
1111 of each of the three different parallel illumination modalities for two-photon voltage imaging. Responses are
1112 reported as the fluorescence change (ΔF) normalized by the baseline fluorescence (F_0), expressed as a
1113 percentage of the baseline fluorescence ($\% \Delta F/F_0$). The average trace and 95 percent confidence interval
1114 from all cells imaged with each modality are plotted (blue – GPC, yellow – Gaussian, red – CGH). The
1115 corresponding electrophysiology control signals are plotted in black. The red bar above the
1116 electrophysiology trace indicates the illumination epoch. **(c)** Quantification of data for all cells from protocol
1117 2. Log(F), SNR, $-\% \Delta F/F_0$, photobleaching and photorecovery are plotted as a function of power density
1118 (power density: 0.66 – 1.55 $\text{mW } \mu\text{m}^{-2}$, 75 – 175 mW per cell, $n = 8 - 13$), see also Supplementary Figure 9.
1119 Each point represents a measurement from an individual cell. The mean is plotted for each condition.
1120 Photostability is defined as the ratio between the integral of the baseline fluorescent trace to $F_0 \cdot n_t$ where F_0
1121 represents the fluorescence in the first frame and n_t the number of baseline fluorescence timepoints (see
1122 schematic diagram, fourth panel, inset). Photorecovery is defined as the average ratio of the fluorescence
1123 prior to the 100-mV depolarization in each illumination epoch (for instance F_1/F_0 as defined in the schematic
1124 diagram, fourth panel, inset). All data was acquired with laser A tuned to 940 nm and camera A (See
1125 Supplementary Figure 1 and Supplementary Tables 1 and 2).

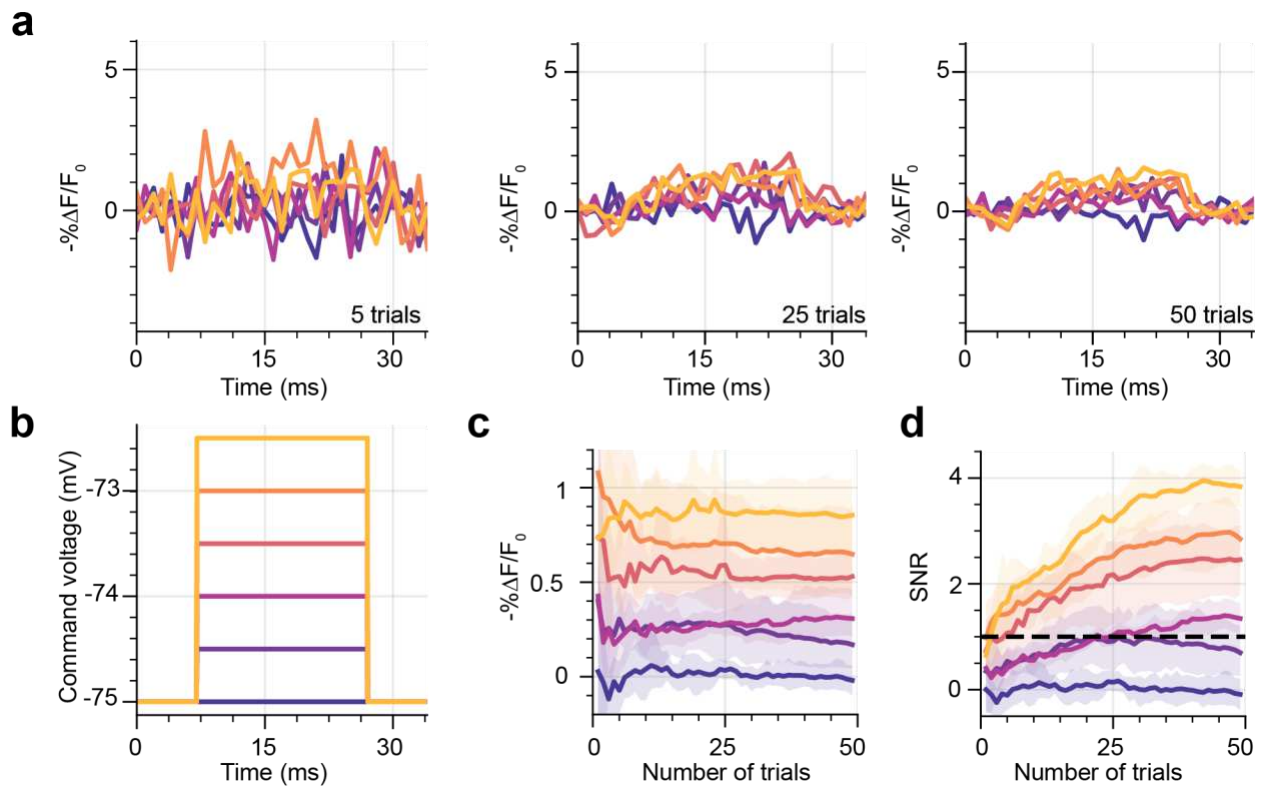
1126



1129 **Recording electrically evoked single action potentials and high-frequency spike trains in JEDI-2P-**
1130 **kv expressing hippocampal organotypic slices with 2P-TF-GPC.**

1131 **(a)** Upper: confocal image of a representative organotypic slice bulk-infected with JEDI-2P-kv. Scale bar
1132 represents 75 μm . Lower: zoom (x2) of densely expressing region where data was recorded. **(b)** Upper:
1133 representative single frame from data acquired with TF-GPC (1 ms exposure time), Lower: line-profile
1134 through the image (indicated by the dashed line) demonstrating that single cells are imaged with high-
1135 contrast in densely labelled samples with 2P-TF-GPC. **(c)** Electrically induced and recorded action
1136 potentials (left) and optically recorded (right) were resolved in single trials using 2P-TF-GPC at different
1137 acquisition rates. Individual trials are plotted in grey. The average trace across all trials is plotted in a
1138 different shade of blue corresponding to each acquisition rate (500 Hz, 750 Hz and 1 kHz, as labelled).
1139 Power density: $1.1 \text{ mW } \mu\text{m}^{-2}$ (125 mW per cell). **(d)** $-\% \Delta F/F_0$ and SNR plotted as a function of power density
1140 in different shades of blue for different acquisition rates (see legend). Error bars represent the standard
1141 error of measurements across all cells ($n = 4-6$). Individual points represent the average value over 50
1142 action potentials for individual cells. All data were acquired using laser A tuned at 940 nm, and camera A
1143 (See Supplementary Figure 1 and Supplementary Tables 1 and 2). **(e)** Representative fluorescence traces
1144 recorded from individual cells to different rates of electrically evoked spike trains recorded at the different
1145 acquisition rates of 500 Hz, 750 Hz and 1 kHz corresponding to 2 ms, 1,33 ms and 1 ms exposure time
1146 (power density: $1.1 \text{ mW } \mu\text{m}^{-2}$, 125 mW per cell). A representative trace of electrically evoked spike trains is
1147 also plotted in black (left). **(f)** $-\% \Delta F/F_0$, SNR, action potential detection probability and precision of action
1148 potential timing estimation (defined as the jitter in timing estimation for all identified action potentials relative
1149 to the corresponding electrophysiological recordings) plotted as a function of power density for different
1150 acquisition rates (500 Hz, 750 Hz, and 1 kHz, see legend). A lower value indicates superior timing
1151 estimation. Data plotted for all train rates ($n = 2-5$). All data were acquired using laser B fixed at 920 nm,
1152 and camera B (See Supplementary Figure 1 and Supplementary Tables 1 and 2).

1153 **Figure 4**

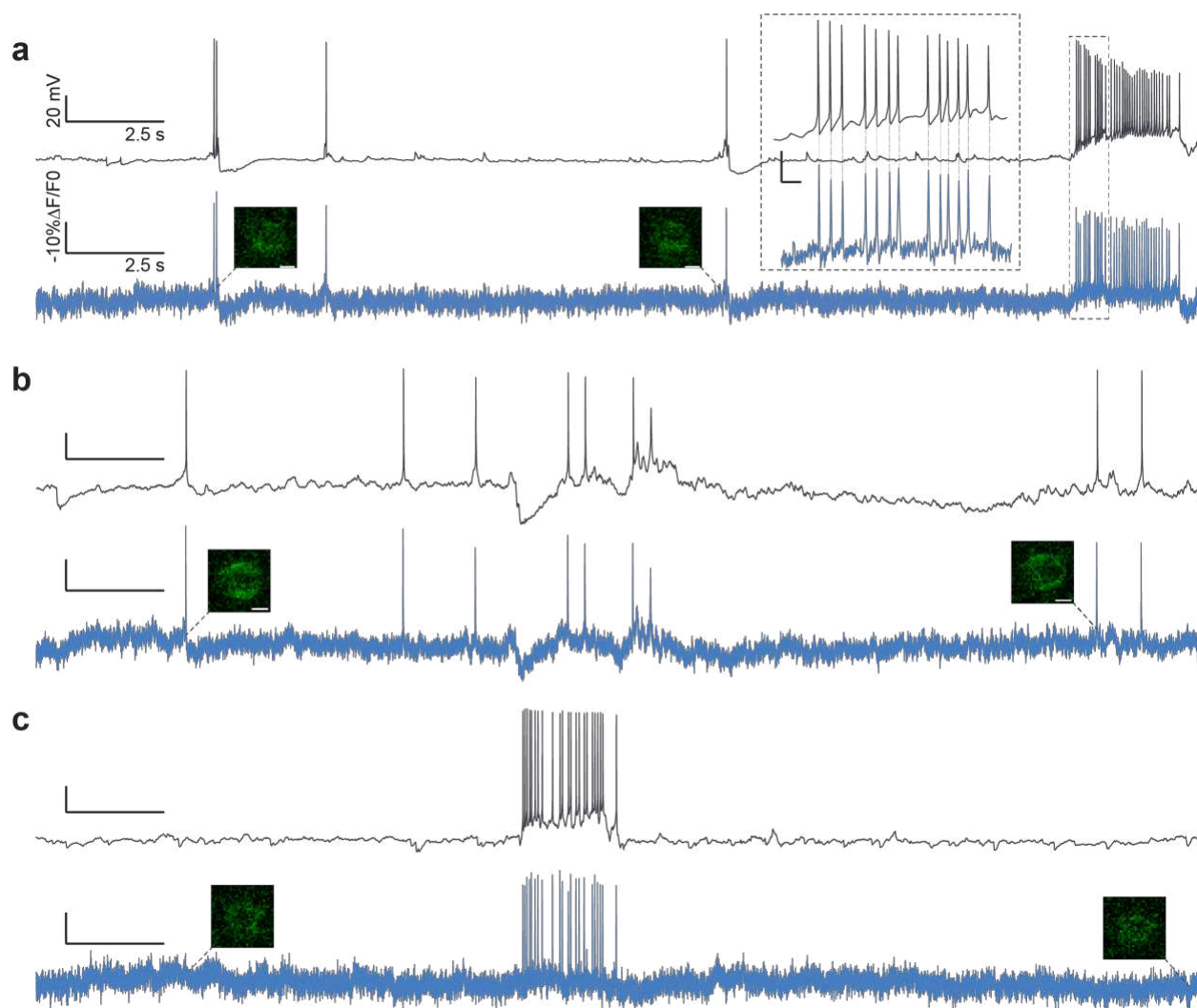


1154

1155 **Recording sub-threshold depolarizations in JEDI-2P-kv expressing hippocampal organotypic slices**
1156 **using 2P-TF-GPC.**

1157 **(a)** Average fluorescence traces recorded from neurons after 5, 25 and 50 trials for different magnitudes of
1158 sub-threshold depolarizations ranging between 0 and 2.5 mV. Sub-threshold depolarisations < 2.5 mV
1159 cannot be reliably resolved in single trials using 2P-TF-GPC and JEDI-2P-kv, however after 25 trials
1160 depolarisations greater than or equal to 1 mV can be resolved. Traces were recorded with a 1 ms exposure
1161 time and $1.1 \text{ mW } \mu\text{m}^{-2}$ (125 mW per cell). **(b)** Command voltage steps used to change the membrane
1162 potential of patched neurons. **(c)** Average $-\% \Delta F / F_0$ and **(d)** SNR of the fluorescence response to different
1163 sub-threshold changes of membrane potential plotted as a function of number of repeats. The 95%
1164 confidence interval is also plotted (shaded region). All data ($n = 6$) were acquired using laser B fixed at 920
1165 nm and camera B (See Supplementary Figure 1 and Supplementary Tables 1 and 2).

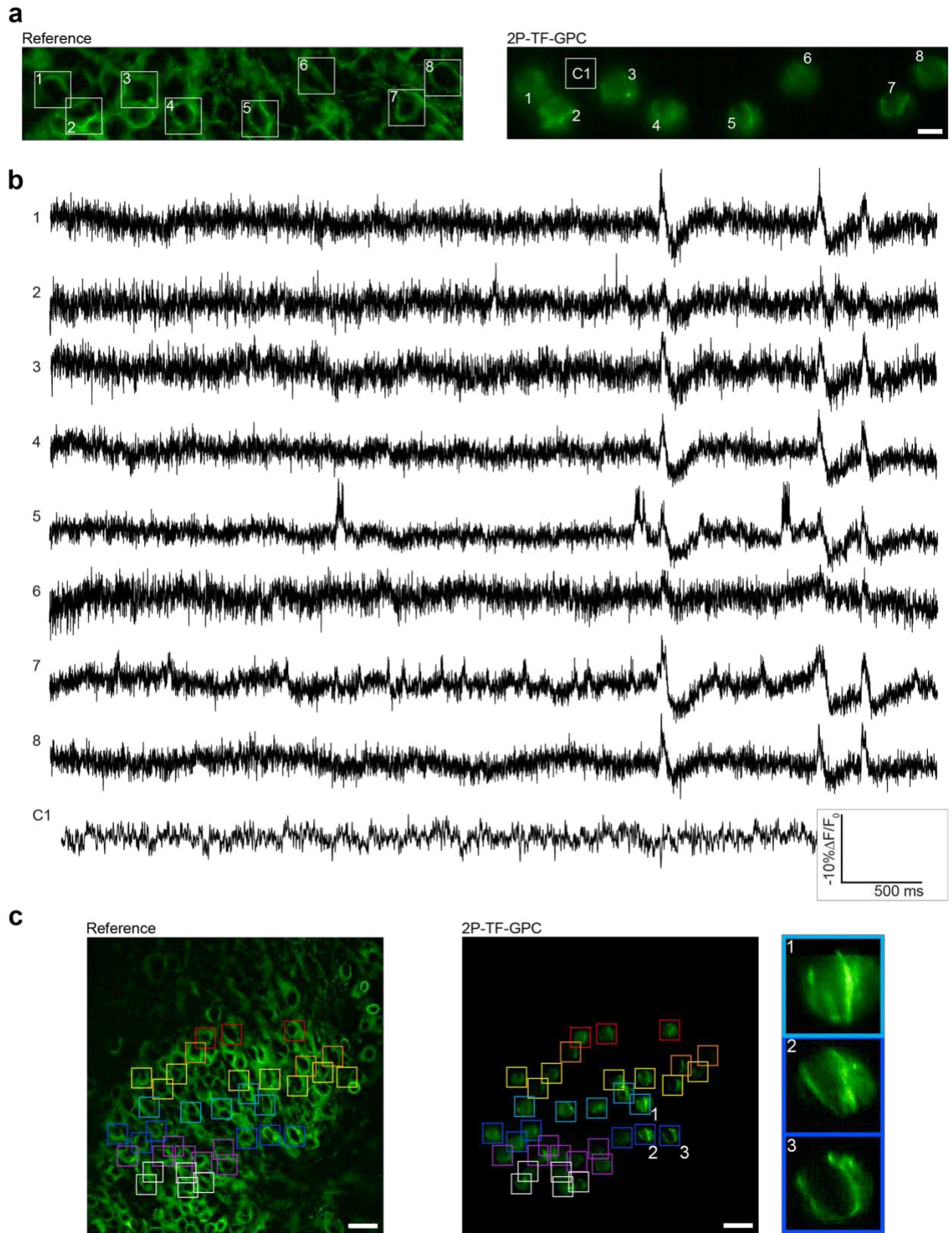
1166 **Figure 5**



1167
1168 **Recording spontaneous neural activity in JEDI-2P-kv expressing hippocampal organotypic slices**
1169 **using 2P-TF-GPC**

1170 **(a-c)** Simultaneous current clamp (upper, black) and fluorescence recordings (lower, blue) of spontaneous
1171 activity in neurons from hippocampal organotypic slices over a continuous 30 s recording period. Single
1172 imaging frames are shown close to the beginning and end of each recording. Scale bars represent 5 μm .
1173 Inset, **(a)** zoomed in portion of the electrophysiological and fluorescence traces. Corresponding action
1174 potentials in the electrophysiological and fluorescence traces (average rate: 17 Hz) is indicated by the
1175 dashed lines. (Power density: $1.33 \text{ mW } \mu\text{m}^{-2}$, 150 mW per cell, 1 kHz acquisition rate). All data was acquired
1176 using laser A tuned to 940 nm and camera A (See Supplementary Figure 1 and Supplementary Tables 1
1177 and 2).

1178

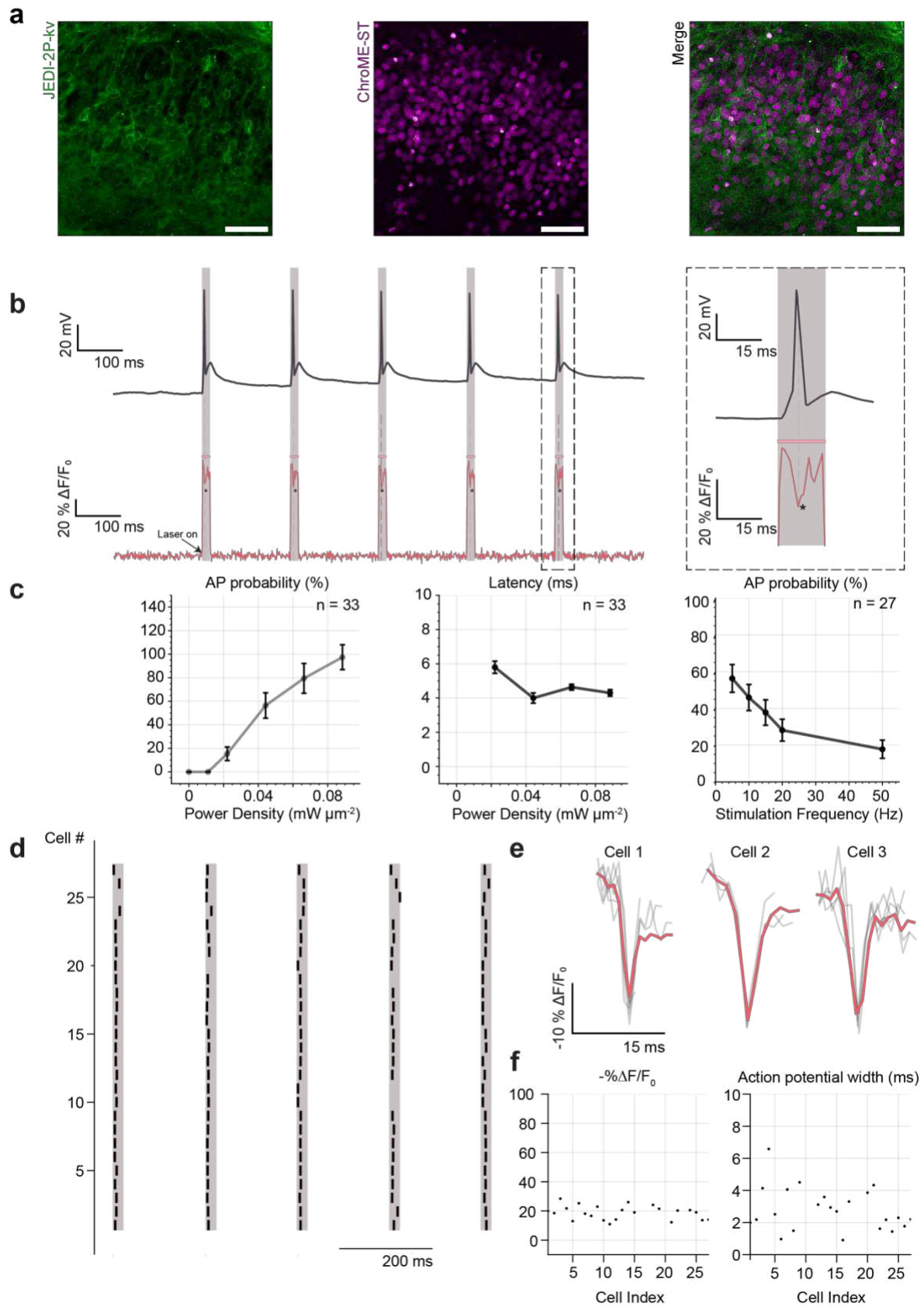


1181 **Multi-cell recordings of spontaneous neural activity in JEDI-2P-kv expressing hippocampal**
1182 **organotypic slices using multiplexed 2P-TF-GPC**

1183 **(a)** Reference image of a hippocampal organotypic slice expressing JEDI-2P-kv in the dentate gyrus (left
1184 panel) and average projection of the corresponding voltage imaging dataset (right panel). 8 neurons
1185 targeted simultaneously with 8, 12- μm 2P-TF-GPC spots can be identified (as numbered and highlighted
1186 by the square boxes). The scale bar represents 10 μm . C1 refers to the area used to generate the control
1187 trace plotted in (b). This ROI was not targeted with a GPC spot during experiments. **(b)** Fluorescent traces
1188 plotted for each of the neurons indicated in (a), including the control trace. **(c)** Voltage imaging throughout
1189 a large field of view using multiplexed 2P-TF-GPC. Left panel: cross-section of a hippocampal organotypic
1190 slice expressing JEDI-2P-kv in the dentate gyrus. Middle panel: combined maximum projections of data
1191 from 7 consecutive acquisitions (indicated by the coloured squares), spanning a total area of 200 x 150
1192 μm^2 . Zoom in for best viewing. Scale bars represent 25 μm . Right panel: zoomed in regions of the central
1193 panel (indicated by numbering and coloured boxes) showing maximum projections of data acquired from
1194 individual cells targeted with multiplexed 2P-TF-GPC. All data was acquired using laser C (940 nm, power
1195 density: 0.02 – 0.09 $\text{mW } \mu\text{m}^{-2}$, 2.5 – 10 mW per cell) and camera A with an acquisition rate of 1 kHz (See
1196 Supplementary Figure 1 and Supplementary Tables 1 and 2).

1197

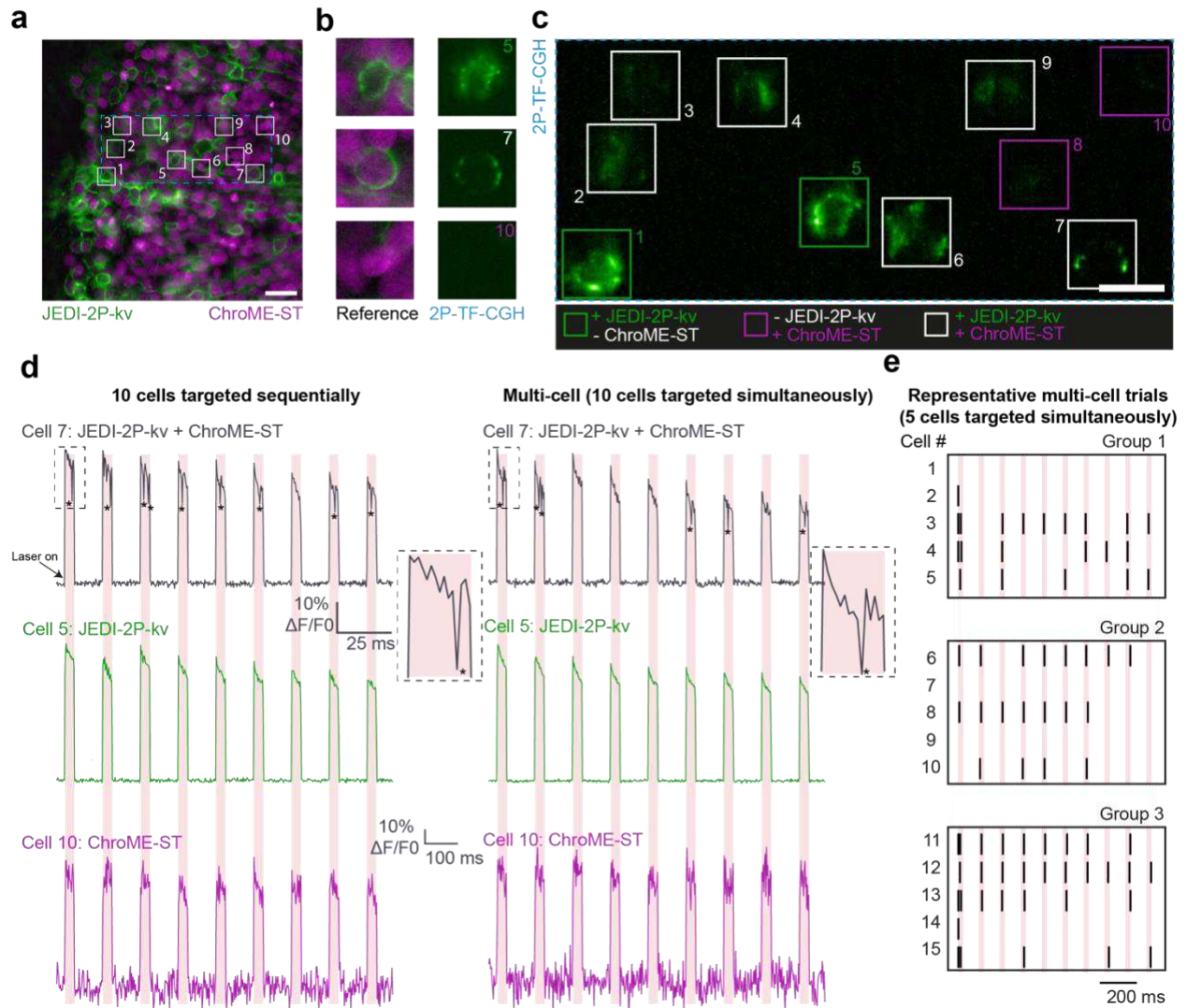
Figure 7



1199 **Fluorescence recordings of photo-evoked spikes in hippocampal organotypic slices co-expressing**
1200 **JEDI-2P-kv and ChroME-ST, using 2P-TF-CGH.**

1201 **(a)** Cross-sections of hippocampal organotypic slices co-expressing the genetically encoded voltage
1202 indicator JEDI-2P-kv and the soma-targeted channelrhodopsin ChroME-ST in the dentate gyrus.
1203 Channelrhodopsin-expressing cells were identified according to their nuclear-localized fluorescence (see
1204 Methods). Scale bar represents 50 μm . **(b)** (left) Simultaneous optical and electrophysiological recordings
1205 demonstrating that action potentials can be evoked and imaged using a single excitation spot (12 μm
1206 diameter, power density 0.02 $\text{mW } \mu\text{m}^{-2}$ (2.5 mW per cell), 15 ms strobed illumination at 5 Hz). (right) Zoom
1207 on simultaneous optical and electrophysiological recordings of one action potential. **(c)** All-optical in-situ
1208 characterisation of photo evoked action potentials. Error bars represent the standard error of recordings
1209 obtained for 33 cells. The probability of evoking and recording action potentials is plotted as a function of
1210 power density. Only cells in which at least one optically evoked action potential was detected are included.
1211 The latency of optically evoked action potentials is plotted as a function of power density. The average
1212 latency measured all-optically matches that obtained using electrophysiology (Supplementary Figure 20c).
1213 The action potential probability is plotted as a function of stimulation frequency. Action potential probability
1214 is calculated as the number of action potentials evoked and recorded over five trials (power density: 0.01 –
1215 0.09 $\text{mW } \mu\text{m}^{-2}$, 1.5 – 10 mW per cell). Error bars represent the standard error of recordings obtained for 33
1216 cells. **(d)** Raster plot of 27 cells showing the number and timing of optically evoked action potentials (black)
1217 relative to the imaging/photostimulation epoch (red) (power density: 0.02 – 0.08 $\text{mW } \mu\text{m}^{-2}$, 2.5 – 9 mW per
1218 cell). **(e)** Examples of fluorescence recordings of optically evoked action potentials for three representative
1219 cells. Individual trials are plotted in grey. The average trace across all trials is plotted in red (power density:
1220 0.02 – 0.08 $\text{mW } \mu\text{m}^{-2}$, 2.5 – 9 mW per cell). **(f)** Summary statistics for the amplitude ($-\% \Delta F/F_0$) and width of
1221 the optically evoked action potentials from (d). All data were acquired using laser C fixed at 940 nm and
1222 camera A (See Supplementary Figure 1 and Supplementary Tables 1 and 2).

1223



1225

1226 **Characterisation of simultaneous multi-target photostimulation and voltage imaging using a single**
 1227 **beam scanless two-photon excitation.**

1228 **(a)** Cross-sections of hippocampal organotypic slices co-expressing JEDI-2P-kv and ChroME-ST in the
 1229 dentate gyrus. The boxes indicate cells that were targeted simultaneously during a representative
 1230 experiment (as numbered). Scale bar represents 25 μ m. **(b)** Reference widefield images of individual
 1231 targeted cells (left) and corresponding images obtained using 2P-TF-CGH. Upper: a cell exclusively
 1232 expressing JEDI-2P-kv. Middle: a cell co-expressing JEDI-2P-kv and ChroME-ST. Lower: a cell exclusively
 1233 expressing ChroME-ST. **(c)** Data acquired when the 10 cells identified in (a) were targeted simultaneously
 1234 using 2P-TF-CGH and imaged at 500 Hz. Scale bar represents 15 μ m. **(d)** Traces from the three cells
 1235 highlighted in (b) when targeted sequentially (left) or simultaneously (right). Of the three selected cells,
 1236 as expected, no action potentials were detected for cell 5 (green) or cell 10 (purple), which did not co-express
 1237 the two constructs. In both the sequential and multi-cell acquisitions, action potentials were only evoked/
 1238 recorded in the cells co-expressing JEDI-2P-kv and ChroME-ST (black). **(e)** Raster plots from 3 further
 1239 experiments in which 5 cells were targeted simultaneously. Black lines indicate the time at which a cell
 1240 fired; the red lines indicate the imaging/photostimulation laser. All data were acquired using laser C fixed
 1241 at 940 nm and camera A (See Supplementary Figure 1 and Supplementary Tables 1 and 2).

Supplementary Files

This is a list of supplementary files associated with this preprint. Click to download.

- [scanlessvoltageimagingssupplementaryinformationfigscaptions.pdf](#)
- [scanlessvoltageimagingssupplementaryinformationfigscaptions.pdf](#)
- [NCOMMS2253557RSC.pdf](#)